UiT
THE ARCTIC
UNIVERSITY
OF NORWAY

Faculty of Science and Technology

Department of Physics and Technology

Oil Spill Analysis Using Hybrid-Polarization Synthetic Aperture Radar

—

Audun Leonard Høifødt

FYS-3921 Master's Thesis in Electrical Engineering, June 2016

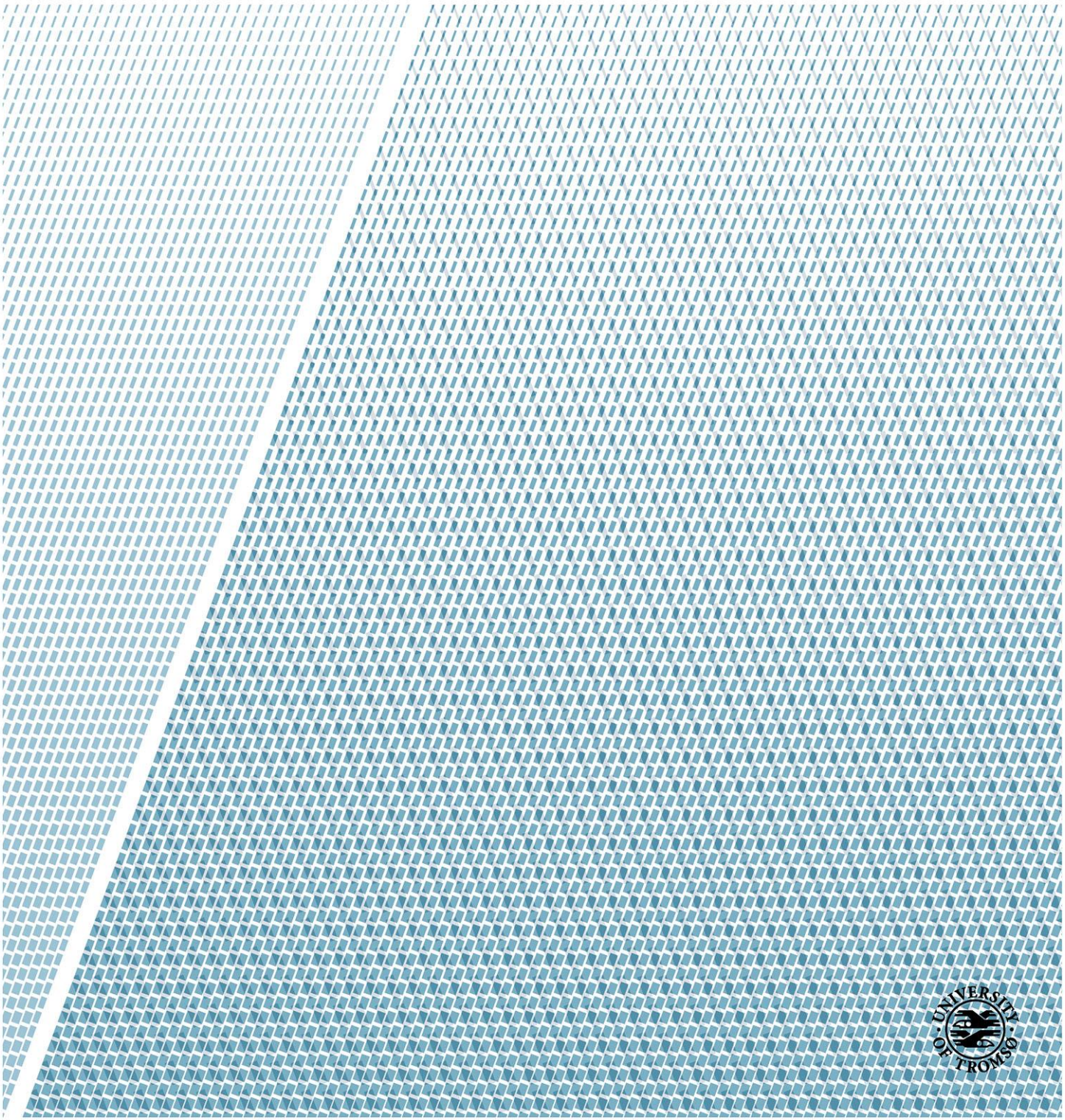

Abstract

Synthetic Aperture Radar (SAR) has over the last few decades become one of the major tools for global environmental monitoring. The need to cover vast areas on a regular and rapid basis, and during all weather and light conditions, make the SAR instrument a natural choice.

Hybrid Polarization (HP) SAR (circular transmit, linear receive) were developed as an alternative to gain either higher resolution or wider swath width, compared to the traditional Quadrature Polarization (QP) and Single-Polarization modes which are commonly used today, while at the same time maintaining as much of the polarimetric information as possible. In addition, HP SAR has the advantage of being relatively easy to implement, it is rotationally invariant, has a low susceptibility to noise and cross-channel errors, and has unique self-calibration features. However, as it is a relatively new mode (2007), the availability of actual HP SAR data has been limited, and consequently most of the existing studies on HP has been performed on HP data simulated from QP.

The goal for this thesis is to test various HP SAR parameters using actual HP data, recorded by the Indian satellite RADAR Imaging Satellite 1 (RISAT-1), and to evaluate the validity of these parameters with respect to oil slick detection. As part of the evaluation, the impact of the system noise and incidence angle on the SAR images is discussed.

It is shown that the signal to noise ratio (SNR) of the sensor has a large impact on the HP mode, and that the Stokes parameters is effective for enhancing the observed features in SAR imagery. The ellipticity parameter is often referred to in the literature as a somewhat unstable parameter for oil slick detection. Also in this thesis, the ellipticity parameter is shown to be a parameter which should be treated with caution until more knowledge about how it responds to the noise and incidence angles.

The best parameter for oil spill detection, was for the evaluated scenes found to be the first Stokes parameter, S_1. In all, the HP mode is found to be a valid mode for oil spill detection, even with low SNR as was the case for the evaluated scenes. However, it is not possible to differ between different types of oil, and/or lookalikes in the scenes that is evaluated in this thesis.

Acknowledgements

First of all, I want to thank my supervisors Camilla Brekke and Stine Skrunes from UiT, and Mari-Ann Moen from Kongsberg Satellite Services AS (KSAT). Your patience, support and feedback, and indeed your very just and timely "pokes" at the times when I faded into my day-job and disappeared from your radar for a while, has been greatly appreciated, and much needed. And a special thank you for proof reading, and for pointing out valuable literature resources.

Thanks to the scientists at the Norwegian Meteorological Institute for providing wind information for scene 2.

A special thanks is required to my fellow student and advisor Martine M. Espeseth for her valuable high spirits and endless inspirational knowledge and interest in SAR technology, which she so willingly share. And an extra thank you for proof-reading.

My employer KSAT also deserves thanks, and especially my Directors Marte Indregard and Mai-Eli Johansen, for pushing me to go through with this, and for allowing me to participate in classes when I really should have been to work.

I also want to thank my colleagues at KSAT in general, and in particular Ole Morten Karlsen for our valuable late-night SAR discussions, long after normal working hours. And I need to thank my colleague Martin Erntsen for setting me up with the mystery of Tex. Although Tex definitely has cost me too many hours, the project would've crashed and burned several times over without your help in this field.

To my parents and to my brother and sister, you should know that your work and achievements in life is a constant inspiration. That you can, enables me.

And to my own Fantastic 4, my wonderful children, I'm sorry for my absense over the past years. I promise to spend much more time with you from now on, all of you. I've missed you all far too much already.

Last, but far, far, far from least, I need to thank my wonderful wife for putting up with me all of these years, even when I *have* been present at home. It is actually you that have done the heavy lifting while I've been busy doing this. Without you, I would not be where or who I am today. This is for you.

Table of Contents

Nomenclature

B	Signal Bandwidth
β_a	Antenna bandwidth in azimuth direction
c	Speed of light in vacuum
χ	Poincaré ellipticity parameter
Coh	Coherence measure
δ	Relative phase
$\Delta\phi$	phase difference
Δt	Time difference
$\mathbf{E}$	Electric field vector
f_0	Transmitted signal frequency
f_D	Doppler frequency
Γ	2×2 Sinclair Matrix
h	Orbital height
H	entropy
j	Imaginary unit ($i^2 = -1$)
$\boldsymbol{J}$	The Jones coherency matrix
L	Antenna length
λ	Wavelength
$m_{\mathbf{C}}$	Degree of circular polarization
$m_{\mathbf{L}}$	Degree of linear polarization
μ	Conformity index
$\mu_{\mathbf{C}}$	Circular polarization ratio
$\mu_{\mathbf{L}}$	Linear polarization ratio
n	The refractive index
P	An observed object
P_e	Power of an electrical wave
ψ	Poincaré orientation parameter
r	The axial ratio of the polarization ellipse
ρ_{CL}	Correlation Coefficient between E_H and E_V

σ_{CPD}	Standard deviation of the co-polarized phase difference
σ_h	Standard deviation of the surface height
$\mathbf{S}$	Stokes vector, a logical vector represented by the four Stokes Parameters: S_1, S_2, S_3 and S_4
τ_p	Transmitted pulse duration
θ_i	incidence angle
v	Speed of satellite
X_a	Resolution in azimuth direction
X_{ground}	Ground resolution across track (range)
X_{slant}	Slant resolution across track (range)

Abbreviations

2D	two dimensional
ALOS	Advanced Land Observation Satellite, aka DAICHI
ALOS-2	Advanced Land Observation Satellite 2, aka DAICHI-2
CC	Dual-Circular
CP	Compact Polarimetry
CPR	Circular Polarization Ratio
CRS	Coarse Resolution ScanSAR mode
d_{norm}	Normalized Difference between Samples
DoC	Degree of Circularity
DoP_c	Degree of circular polarization
DoD	Degree of Depolarization
DoP_l	Degree of linear polarization
DoP	Degree of Polarization
DP	Dual-Polarization
DWH	Deep Water Horizon
EM	Electromagnetic
EM20	Oil Emulsion containing 20 % water
EM40	Oil Emulsion containing 40 % water
EM60	Oil Emulsion containing 60 % water
FP	Fully Polarimetric
FRS-1	Fine Resolution Stripmap mode
HH	Horizontal transmit, Horizontal receive
H	Horizontal
HP	Hybrid Polarization
HV	Horizontal transmit, Vertical receive
IPP	Inter-Pulse Period
LCTLR	left circular transmit, linear receive

LPR	linear polarization ratio
LWR	low-wind region
$m - \alpha$	$m - \alpha$ decomposition
$m - \chi$	$m - \chi$ decomposition
$m - \delta$	$m - \delta$ decomposition
$m - \psi$	$m - \psi$ decomposition
MRS	Medium Resolution ScanSAR mode
NESZ	noise equivalent sigma zero
NISAR	NASA-ISRO Synthetic Aperture Radar
NOFO	Norwegian Clean Seas Association for Operating Companies
NRCS	Normalized Radar Cross Section
OLA	Oleyl Alcohol
OoW	Oil on Water
$\pi/4$	$\pi/4$ compact polarimetry mode
PRF	Pulse Repetition Frequency
QP	Quadrature Polarization
Quasi-QP	Quasi-Quadrature Polarization
RAR	Real-Aperture Radar
RCTLR	right circular transmit, linear receive
RISAT-1	RADAR Imaging Satellite 1
rms	root mean square
RADARSAT-2	RADAR Satellite 2
SAOCOM-1	Satélite Argentino de Observación Con Microondas 1
SAR	Synthetic Aperture Radar
SIR-C/X-SAR	Spaceborne Imaging Radar-C/X-band Synthetic Aperture Radar
SNR	signal to noise ratio
SP	Single-Polarization
SLC	Single-Look Complex
V	Vertical
VH	Vertical transmit, Horizontal receive
VV	Vertical transmit, Vertical receive
WWII	World War II
X-Bragg	extended Bragg
"RCM"	RADARSAT Constellation Mission

Glossary

ALOS-2, aka DAICHI-2

The successor of the Japanese ALOS satellite, also known as DAICHI, ALOS-2 is also known as DAICHI-2. The predecessor ALOS was one of the giants within the global monitoring field, due to it's multi-sensor capabilities. Flying from 2006, operation was ended in 2011. ALOS-2 was planned to release ALOS in 2011, but the launch was delayed until May 24, 2014

ESA

The European Space Agency. With 22 member nations and 8 cooperating nations, ESA is the major architect and executor of the European space programme. From their headquarters in Paris, operations are spread across Europe, employing ~2200 people at multiple locations in several nations. Their budget of €4020 million (2012 numbers) is invested in each member state through industrial contracts for space programmes in approximately similar amounts as the member states contributes with.

LRO

The Lunar Reconnaissance Orbiter, a NASA mission to observe the moon as preparation for future robotic and manned moon landings. The orbiter entered lunar orbit on June 23, 2009, and is still flying. The onboard sensors will generate a global moon map, pinpoint possible secure landing sites, look for resources (e.g. water), measure the radiation from space to predict the effect on humans, and measure light and temperature on the moon's poles.

MiniRF

The Miniature Radio Frequency instrument is a Synthetic Aperture Radar with Hybrid Polarization mode capability. Two missions have so far carried an instrument from the Mini-RF project; The Indian Space Research Organisation's (ISRO's) Chandrayaan-1 spacecraft and NASA's Lunar Reconnaissance Orbiter (LRO).

PolSARpro

The Polarimetric SAR data Processing and Educational Toolbox. A software developed since 2003 under ESA-ESRIN contracts. The contractor being ESA-ESRIN Science Application and Future Technologies Dept, Research Development Section, and the principal investigator being I.E.T.R at the University of Rennes. The version used in this thesis is version 5.0.4 (January 2015).

"RCM"

The RADARSAT Constellation is planned to further develop the already on-going RADARSAT mission, currently covered by RADARSAT-2. The first satellite is planned to be launched in 2018, and so as to avoid any data gap after the RS-2 end of life. The constellation will contrary to it's predecessors consist of 3-6 satellites, to increase revisit capabilities, orbital control etc. It will however, continue the RADARSAT tradition of carrying a C-band SAR sensor.

RISAT-1

An Indian C-band SAR Earth Observation Satellite, built and operated by the Indian Space Research Organisation (ISRO).

RADARSAT-2

A Canadian C-band SAR Earth Observation Satellite, operated by MacDonald, Dettwiler and Associates Ltd. (MDA). Launched 14 December 2007 as a successor to RADARSAT-1.

UAVSAR

The UAVSAR is intended to be carried by a UAV (Unpiloted Aerial Vehicle), though it is initially demonstrated mounted on a Gulfstream III aircraft (C-20A/GIII). That means that the system nominally will operate at lower altitudes (13,800 m). The SAR instrument operates at L-band frequency, at approximately 1.26 GHz.

List of Figures

List of Tables

Chapter 1

Introduction

Oil spills at sea, whether accidental or intentional, represent one of the most important and dramatic threats to the marine environment worldwide. The ripples of disasters such as the Exxon Valdez (1989), the Prestige tanker accident (2002) and the more recent Deep Water Horizon (DWH) (2010) all had a severe impact, and to some degree still have in the respective surrounding areas[26,39]. Truth be told, the latest official reports from Exxon Valdez now reveals that the oil, although still present, is no longer bioavailable and that the key injured resources are no longer being affected by the lingering oil[8]. Along with the continuous work to prevent future disasters from happening, it is crucial to improve the existing oil spill preparedness, in order to be able to react quickly and efficiently, and be able to distinguish actual threats from false alerts. As part of this, efficient and frequent monitoring of ships as well as permanent installations such as pipelines and oil rigs, is a challenge of utmost importance.

Space-borne Synthetic Aperture Radar (SAR) instruments offer a valuable tool for this purpose. As they are virtually unaffected by both weather and lighting conditions, they can operate under most conditions, and reach areas that would otherwise be difficult or impossible to cover. This is particularly valuable in remote areas, areas frequently covered by clouds, or e.g. in the Arctic regions during the polar night.

SAR resolution is directly linked to ground coverage, which means that if high resolution is required, the ground coverage will be less, and conversely. The different available acquisition modes will either favour resolution or ground coverage, and the choice of mode is therefore important. Quadrature Polarization (QP) SAR both transmits and receives in two polarizations. This offers valuable polarimetric

information about the observed target, but suffers from small ground coverage due to transmitting in interleaved polarizations. To compensate for the lesser ground coverage, either the antenna would have to be doubled in length, or the Pulse Repetition Frequency (PRF) would have to be doubled in order to sample the backscatter at a sufficient rate. However, this causes the Inter-Pulse Period (IPP) to be halved, which then reduce the swath width to at least half of what is available for the same system operating in Dual-Polarization (DP) mode. This could also introduce range ambiguities which may further reduce the swath width, particularly at high incidence angles[38]. DP mode on the other hand, does not offer the same amount of polarimetric information. Today, Single-Polarization (SP) is the most used mode for oil spill detection, due to the large ground coverage

During the last decade a new set of modes named Compact Polarimetry (CP) has been suggested as a compromise between traditional DP mode and QP. In principle, CP is in fact a version of DP mode, but rather than transmitting in the traditional Horizontal (H) or Vertical (V) polarizations, CP transmits in either diagonal polarization or in circular polarization, known as the $\pi/4$ compact polarimetry mode ($\pi/4$) or Hybrid Polarization (HP), respectively. While keeping the relative light-weight and simple construction of DP instruments, CP allows reconstruction of a pseudo QP covariance matrix, thus achieving nearly as rich data as from QP without loosing ground coverage. According to Raney et al.[38], HP also benefits from improved range ambiguity performance compared to QP, and it requires half the average transmit power compared to QP[5].

The interest for the HP has been increasing since it's publication in 2007, and the literature is more or less in agreement about the superiority of HP in comparison to other CP modes. Applications such as oil spill detection and characterization, ship detection, crop monitoring, interferometry and natural disaster alerts (e.g. landslides, floods etc.) have all been investigated.[2,7,14,16,17,19,22,23,40,42,43,46,50]

In the near future, several missions are planning to include HP mode as part of their sensor capability. The Satélite Argentino de Observación Con Microondas 1 (SAOCOM-1) scheduled for launch in 2016 and 2017 (SAOCOM-1A and SAOCOM-1B, respectively), the American-Indian joint mission NASA-ISRO Synthetic Aperture Radar (NISAR), which is scheduled for 2019/2020, and the Canadian "RADARSAT Constellation Mission" scheduled for launch in 2018, have all announced that they will carry an HP sensor.

Currently, Advanced Land Observation Satellite 2, aka DAICHI-2 (ALOS-2) (L-band) and RADAR Imaging Satellite 1 (RISAT-1) (C-band) are the only operational CP systems, both carrying a HP instrument. In this thesis, data from RISAT-1 will be used.

1.1 Objective

There has already been performed several studies on Hybrid Polarization (HP) Synthetic Aperture Radar (SAR) for the application of oil spill detection on the sea surface, but very few of these have had access to actual HP data. The development and evaluation of techniques and parameters has therefore been performed using HP data simulated from Quadrature Polarization (QP) data. It is thus urgent to test these parameters and methods on real HP data, to verify their validity.

The objective of this thesis is to test various HP parameters for oil spill analysis, using actual HP data recorded by RADAR Imaging Satellite 1 (RISAT-1). The parameters that will be evaluated are the individual Stokes parameters, the Degree of Polarization (DoP), the χ and the H. One decomposition, the $m-\chi$ decomposition ($m-\chi$) decomposition, will also be considered. As part of the evaluation, the effect of the system noise and the incidence angle will be discussed.

Two HP Fine Resolution Stripmap mode (FRS-1) scenes from RISAT-1 will be used for the analysis.

1.2 Structure

This thesis is divided into 7 chapters including the introduction.

Chapter 2 contains a brief introduction to remote sensing, with information about the imaging geometry, resolution and polarimetry of SAR.

Chapter 3 is concentrating on polarimetry, describing the scattering mechanisms and the Stokes parameters. The chapter ends with a description of quadrature and hybrid polarimetry.

Chapter 4 lists the parameters that will be discussed in this thesis. Then, the theory of the individual parameters are briefly explained, and previous relevant work is described.

Chapter 5 describes the data sets that has been used.

Chapter 6 presents and discusses the results found during the work with this thesis. It begins by describing the noise analysis that was performed, then moves on to explaining the theory for the statistical distance measure (Normalized Difference between Samples (d_{norm})) that has been used to evaluate the HP parameters,

as well as listing the d_{norm} values. Next, the different evaluated parameters are explained and the results presented and discussed. Finally, a short comparison of the parameters is presented.

In chapter 7, the conclusion is given, and future work is suggested.

In this thesis, the following notations have been used:

- *Figures* are referenced as a set of two arabic numerals in the format <chapter>.<figure number>, but not necessarily being enclosed in parenthesis. E.g. the reference "figure 2.4", will point to the second figure in chapter 2.
- References to *literature* will be written either with the author's name and an elevated reference number, e.g. Raney et al.[37] or just as an elevated reference number enclosed in square brackets[37]. The number corresponds to the reference list that is found at the very end of this thesis.
- *Equations* will be referenced to by a set of two arabic numerals enclosed in parenthesis, in the format (<chapter>.<equation number>). E.g., the equation number (4.2) points to the second equation in chapter 4.
- *Vectors* are written in **bold**, e.g. $\mathbf{S}$.
- *Matrices* are noted in ***bold italic J***

Chapter 2

Synthetic Aperture Radar Imaging for Oil Spill Detection

Remote sensing has played an ever increasingly important role ever since the development of photography. Daguerre and Niepce are credited with the first photographies as far back as in 1839. Ten years later, Colonel Laussedat, used photography for topographical mapping. Then, in 1858, photographies of large areas were achieved by the use of balloons, and by the 1880's cameras were also attached to kites and pigeons to achieve even higher altitudes, and thus larger ground coverage. It was only natural that aeroplanes would be used for aerial photography, and Wilbur Wright is credited with the first photograph taken from an aeroplane. [11]

Color photography and near-infrared sensitive films were developed in the mid-1930's, and during World War II (WWII), research upon the reflectance properties of natural terrain in order to spot camouflaged objects were initiated. Culminating in the launch of the multispectral imagers onboard the Landsat satellites in the 1970's, numerous studies into the application of color infrared and multispectral photography sponsored by NASA was performed starting in the mid-1960's. [11]

Active microwave sensors (radars) have been around since the beginning of the last century, and increasingly so after WWII. Then, the main purpose was to track ships, and eventually also planes. Later, active microwave sensors have been developed to create two dimensional (2D) images which resemble optical photographs, but where the brightness is a representation of the intensity of the backscattered signal from the observed area. There are also passive instruments that measure the natural microwave emission from natural objects. [11]

By the mid-1950's, airborne Real-Aperture Radar (RAR) sensors was being developed. And at approximately the same time, development of SAR was initiated.[11]

Which brings us more or less to the current age, where different modes of SAR are being extensively used for oil spill detection, in addition to numerous other monitoring purposes, both on- and off shore. In the last decade, the introduction of Compact Polarimetry (CP) SAR is added to the Fully Polarimetric (FP), Dual-Polarization (DP) and Single-Polarization (SP) modes. CP was initially introduced by Souyris et al.[46], who suggested the $\pi/4$ compact polarimetry mode ($\pi/4$) mode. Later, Raney[35] proposed the HP mode, which transmits in circular polarization. In addition, there is the alternative of Dual-Circular (CC) SAR, which both sends and receives circular polarized signals, but this is harder to implement, and does not offer additional features compared to the circular-linear option of HP[29]. To the knowledge of the author, it has therefore not been implemented in any existing systems.

The benefit of SAR in oil detection is obvious. The frequency for which it operates allows for penetration of clouds, while receiving polarized backscatter offer information on the physical properties of the observed target. The active instrument technology means that the sensor is not dependent on external illumination, but operates in all light conditions.[18] In addition, there is the large ground coverage capacity and relatively rapid revisit frequency, which allows for frequent monitoring of vast areas that would otherwise be much more inaccessible.

SAR sensors are sensitive to the capillary waves on the sea surface. The sea surface is actually consisting of very small scale waves (Bragg) in addition to the larger waves we tend to observe visually. These small waves are effectively dampened by oil slicks that float on the ocean surface, therefore the backscattered response is much less over oily surfaces than over clean sea[12,48]. The backscattered intensity can then be displayed as an image, where the oil typically will be displayed as a dark patch on a brighter clean sea surface.

A problem arises when other phenomena affect the capillary waves. That could be low-wind region (LWR), other types of naturally occurring floating objects (e.g. algae, fish oil), or similar. If all that is available is the backscattered intensity, these phenomena will appear very similar to oil on the sea surface, hence make it difficult to firmly establish if what is seen is actually oil[3]. Studies have shown that it is still possible to give an improved prediction based on previous experience, statistics and similar, even from SP images[45], and indeed a trained operator can from his/her experience tell oil from look-alike's with relatively high accuracy (the author is himself trained as an oil spill analyst at Kongsberg Satellite Services AS (KSAT)). However, by adding the polarimetric data to the analysis, it may

be possible to extract even more information from the backscatter, and ideally it may be possible to separate oil from other similar-looking objects. It may even be possibly to detect such details as thickness of the oil, concentration, oil type etc., to add to the analysis[44].

Polarimetry represents an additional information carrier to the frequency content and intensity[49], and will be further discussed in chapter 3. In the following sections, the image geometry, frequency and resolution related to SAR will be outlined.

2.1 Imaging Geometry

A SAR instrument measures the reflected and refracted signal backscattered from a target area to make a 2D image of the covered surface. As the sensor moves over the ground, it sends pulses of Electromagnetic (EM) radiation, and measures the echo. In simple terms, as the sensor moves over the ground along a comparably straight line, the radar beam sweeps the ground at approximately the same speed, emitting short EM pulses. The echo is measured and placed in the 2D image according to the current position of the satellite. This gives the image's y-direction, or azimuth direction. The second direction corresponds to the time it takes for the emitted EM pulse to return to the sensor. This yields the image's x-direction, and is generally referred to as the range direction. Geometric distortion caused by the side-looking orientation of the sensor, and that the beam is not absolutely perpendicular to the motion vector of the sensor, is aptly corrected during the processing[9].

Figure 2.1 illustrates the geometry of a SAR system. The figure is inspired by figure 1.1 in the book by Lee and Pottier[18]. The blue rectangle models the SAR antenna with width W_a and length L, while the green strip with width W_g is the ground swath that is recorded by the sensor, where the blue ellipse is the at any instant covered "footprint" (i.e. what the satellite "sees" at that given point in time). It is worth noticing that the swath is placed some degrees to the side of the satellites ground track. Hence, a SAR instrument is referred to as a "side-looking" sensor. The part of the swath that is closest to the satellites ground track, is referred to as near range, while the part furthest away is named far range. h is the orbital height, and the satellites velocity equals v. The signal is sent as "chirps" (see chapter 2.3.1) with pulse length $c\tau$, at an look-angle θ. The look-angle is the angle between the local vertical and the centre line through the viewed cone (marked in blue lines). As a result of the antenna aperture in range direction, the look-angle range is given as $\theta_v \approx \lambda / W_a$, where λ is the wavelength of the transmitted signal.

The resolution in range and azimuth is X_r and X_a, respectively. The resolution will be further discussed in chapter 2.3.1 and 2.3.2.

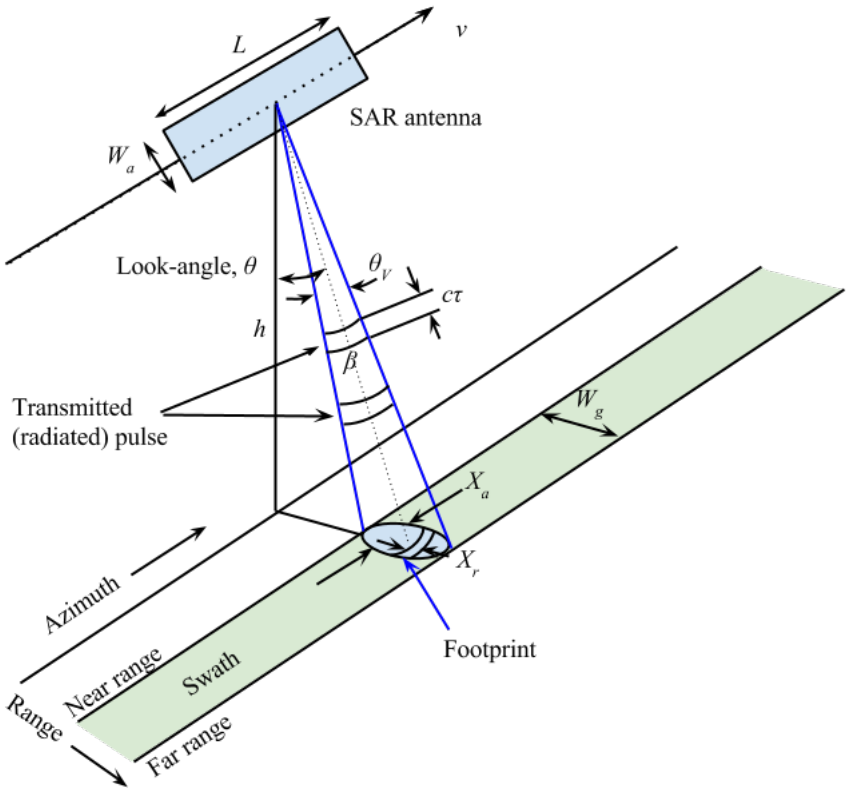

Figure 2.1: Synthetic Aperture Radar geometry (Illustration inspired by Lee and Pottier [18]). h represents the orbital height, W_a and L are the width and the length of the SAR antenna, respectively. $c\tau$ is the chirp pulse length. β is the bandwidth. X_a and X_r are the resolution in azimuth and range, respectively. W_g is the width of the covered swath, and v is the velocity of the satellite. θ is the look-angle (i.e. the angle between the local vertical and the centre line through the viewed cone). θ_v is the look-angle range, corresponding to the antenna aperture in range direction ($\approx \frac{\lambda}{W_a}$, where λ = wavelength).

2.2 Frequency

SAR instruments operates in the microwave region, e.g. on frequencies from about 300MHz to 300 GHz. The microwave region is further divided into several bands, given in table 2.1.

Table 2.1: Microwave spectral bands, with reference to SAR instruments. Slightly updated from Schowengerdt [41].

Band	**Frequency (GHz)**	**Wavelength (cm)**	**Sensors (frequency in GHz)**
Ka	26.5 - 40	0.8 - 1.1	SSM/I (37.0)
K	18 - 26.5	1.1 - 1.7	SSM/I (19.35,22.235)
Ku	12.5 - 18	1.7 - 2.4	Cassini (13.8)
X	8 - 12.5	2.4 - 3.8	X-SAR(9.6), Terrasar-X (9.6)
C	4 - 8	3.8 - 7.5	SIR-C (5.3), ERS-1 (5.25), RADARSAT-1/2 (5.3), RISAT-1 (5.35), Sentinel-1 (5.405)
S	2 - 4	7.5 - 15	Magellan (2.385) (also frequently used for *uplink* and *tracking* purposes)
L	1 - 2	15 - 30	UAVSAR (1.26), PALSAR (1.27)
P	0.3 - 1	30 - 100	NASA/JPL DC-8 (0.44)

For sea surfaces and oil slick detection, the most commonly used bands are L-, C- and X-band.

Long wavelengths will penetrate deeper into the surface compared to shorter wavelength, while radar waves with short wavelengths will respond to the roughness of the surface on a more detailed level than radars with longer wavelengths. How smooth or rough a surface is (i.e., from an electromagnetic point of view), can be decided through a number of different criteria [13,47,49]. But before looking at some of these, the phase difference between two backscattered rays from two separate surface points $\Delta\phi$ needs to be defined [13]

$$\Delta\phi = 2\sigma_h \frac{2\pi}{\lambda} \cos\theta_i \tag{2.1}$$

where σ_h is the standard deviation of the (roughness) height regarding to a reference height, and θ_i is the local incidence angle.

The most commonly used criterion is the *Rayleigh* criterion, which classifies the surface as rough, thus act as a diffuse reflector (see figure 3.1c), if the root mean square (rms) height exceeds one-eighth of the sensing wavelength [24,49], i.e.,

$$\sigma_h > \frac{\lambda}{8\cos\theta_i} \tag{2.2}$$

where λ is the wavelength. This corresponds to $\Delta\phi < \pi/2$.

A more stringent definition of roughness adapted for the EM wave region, is the *Frauenhofer* criterion, was suggested by Ulaby et al.[47] in 1982. According to the Frauenhofer criterion, a surface is considered smooth when $\Delta\phi < \pi/8$, or[47]

$$\sigma_h < \frac{\lambda}{32\cos\theta_i} \tag{2.3}$$

Peake and Oliver[31] suggested yet another approximation, where the surface would be considered rough if

$$\sigma_h > \frac{\lambda}{4\cos\theta_i} \tag{2.4}$$

and smooth if

$$\sigma_h < \frac{\lambda}{25\cos\theta_i} \tag{2.5}$$

If a surface lies between these two σ_h-values, it is considered to have an intermediate roughness[49].

As seen in table 2.1, high frequency corresponds to shorter wavelengths and vice versa. The short wavelength bands (Ka, K, Ku) are more prone to be affected by atmospheric conditions than longer wavelengths, as they are less able to penetrate clouds and rain. The L- and P-bands, representing longer wavelengths, are less influenced by weather conditions, but significantly more affected by the electrons in the ionosphere, which may cause changes in the polarization state of the transmitted waves[18,46]. Because of their compromising nature with regard to weather and ionospheric penetration, X- and C-band are often preferred for earth observation satellites (depending on application)[4], although X-band is more affected by weather conditions[10].

2.3 SAR Resolution

The resolution of a SAR instrument is defined as the sensors ability to clearly distinguish between two adjacent targets both in range and in azimuth direction. As the sensor is constantly moving, the definition of the resolution is different in the direction of the satellites movement (along-track/azimuth), and in the direction perpendicular to the satellites movement (across-track/range). This is further explained in the following sections.

2.3.1 Range Resolution

In range (across track), it is common to refer to either slant range resolution or ground range resolution. Both are measures for spatial resolution, and the relationship between the two is defined as[18]

$$X_{ground} = \frac{X_{slant}}{\sin\theta_i} \tag{2.6}$$

where X_{ground} is the ground range resolution, X_{slant} is the slant range resolution, and θ_i is the local incidence angle.

The slant range resolution is defined as[18]

$$X_{slant} = \frac{c}{2B} \tag{2.7}$$

where c is the speed of light in vacuum, and B is the system bandwidth.

It is easily seen from equation 2.6 that the ground range resolution will vary across-track non-linearly.

Inserting equation 2.7 into equation 2.6 gives the ground range resolution

$$X_{ground} = \frac{c}{2B\sin\theta_i} \Rightarrow \frac{2X_{ground}\sin\theta_i}{c} = \frac{1}{B} = \Delta t \leq \tau_p \tag{2.8}$$

where Δt time separation of the observed objects, and τ_p is the pulse length.

To distinguish between two objects with a radar, it is important to sample at a sufficiently high rate (i.e. a high Pulse Repetition Frequency (PRF)). However, very short, high energy pulses are difficult to achieve in practice. Therefore, it is common to use a so-called "chirp", which is a long pulse for which the signal frequency is being linearly modulated while the pulse is transmitted. Say that the frequency within the chirp is linearly changed from f_0 to $f_0+\Delta f$, then the effective bandwidth would be[18]

$$B = |(f_0 + \Delta f) - f_0| = |\Delta f| \tag{2.9}$$

From this equation, it is seen that the bandwidth is independent of the pulse length τ_p. The frequency at any given time, is then[49]

$$f(t) = f_0 + \frac{B}{\tau_p}t \qquad \text{for} \qquad -\frac{\tau_p}{2} \leq t \leq \frac{\tau_p}{2} \tag{2.10}$$

If two objects are separated by less than the physical length of the signal pulse, it is not possible to distinguish between them if the frequency of the pulses are the same at all times. This is however overcome using chirps, as the echoes from the two objects will then have different frequency at any given time. Different frequencies can easily be distinguished through frequency filtering, hence the pulse length can be increased (i.e. energy increased) beyond the physical distance between the two neighbouring observed objects. In other words, it is possible to send overlapping chirps as long as the received pulse frequencies at any given time is different. The linearly varying frequency within each chirp make sure that the frequencies of the individual chirps (and returns) never overlaps[11].

So, long pulse duration means high energy, while a wide system bandwidth infers high range resolution. Interestingly, it is also seen that the range resolution is independent of the distance between the observed surface and the sensor, but solely depend on the system bandwidth.[11]

2.3.2 Azimuth Resolution

The resolution in azimuth for a RAR will depend on the width of the antenna footprint, as the echoes from all points along an observed line in azimuth will be received at the same time at the antenna. Consequently, using RAR, the azimuth resolution is given by

$$X_a = \frac{h\beta_a}{\cos\theta} = \frac{h\lambda}{L\cos\theta} \tag{2.11}$$

where h is the shortest distance between the surface and the sensor (orbit height), β_a is the antenna beam width in azimuth direction, λ is the wavelength of the transmitted signal, and L is the length of the antenna.
The problem with this geometry is the fact that space-borne instruments travel at a considerable height, meaning that even with a very short wavelength, the X_a will be intolerably high.

Enter the SAR instrument. In the azimuth direction, there is no change in the distance to the target, such as in range (except perhaps due to topographical changes in the observed area, which is usually negligible). For SAR, the antenna length is synthesized, which can be explained with the Doppler synthesis approach (the synthetic array approach is another way of explaining azimuth resolution for SAR which gives equal results)[11].

From Doppler's theories we know that when a radar is passing an object, P, the echo from P will initially have a positive Doppler shift as P enters the beam, that then decreases down to zero before becoming increasingly negative by the time P exits the beam (see figure 2.2). This fact is utilized to improve the resolution in azimuth.

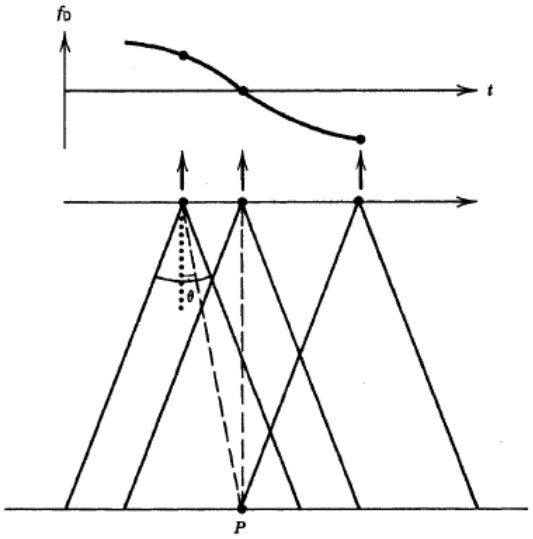

Figure 2.2: Doppler history of a point target P as the SAR sensor passes over it. (Illustration borrowed from Elachi and van Zyl[11])

The object P is seen to have an echo ranging from f_0 (the transmitted signal

frequency) to f_D, which is given by[11]

$$f_D = \frac{2v}{\lambda} \sin\frac{\theta}{2} \simeq \frac{v\theta}{\lambda} = \frac{v}{L} \tag{2.12}$$

where v is the speed of the satellite.

Considering two objects P_1 and P_2 placed a distance X_a apart in the azimuth direction, the Doppler history from object P_2 will be a replication of the one from object P_1, but displaced in time by $t = X_a/v$. The shortest possible time displacement that can be measured after processing the signal with a bandwidth $B_D = 2f_D$ is then given by[11]

$$t_m = \frac{1}{B_D} = \frac{1}{2f_D} = \frac{L}{2v} \tag{2.13}$$

which makes it possible to calculate the highest possible resolution[11]:

$$X_a = vt_m = \frac{L}{2} \tag{2.14}$$

In real life though, SAR sensors sends a series of pulses, not a continuous signal, hence the PRF should be sufficiently high to ensure that the Doppler spectrum is adequately sampled. From equation (2.12) and the Nyquist sampling criteria, we know that

$$PRF > 2f_D = \frac{2v}{L} \tag{2.15}$$

if we assume a carrier frequency which is down-converted to 0. If however, we have a carrier frequency down-converted to f_D, then the minimum PRF will be twice of what is shown in equation (2.15)[11].

From this, it is clear that the PRF is one of the limiting factors with regards to azimuth resolution. In fact, this is one of the reasons for developing CP, as one of the major limitations with QP is the low achievable resolution compared to SP and DP modes.

Chapter 3

SAR Polarimetry

Polarization is the orientation of the EM field, and it is contained in the elements of the vector amplitude of the electric field[49]. In SAR technology, the polarization of the backscattered signal yields added information about the target, depending on the transmitted polarization. The physical properties of the observed targets decides how the transmitted wave is affected, thus there will be polarimetric "signatures" for specific objects.[11]

In a QP system, four channels, i.e. four combinations of transmitted and received polarizations are achievable, namely Horizontal transmit, Horizontal receive (HH), Horizontal transmit, Vertical receive (HV), Vertical transmit, Horizontal receive (VH) and Vertical transmit, Vertical receive (VV). This is also referred to as FP SAR, as this represents all polarization combinations achievable from a linear SAR system[11]. QP will be detailed in section 3.3.

If two polarization channels are being used, the sensor is referred to as a DP system. A DP SAR instrument uses one polarization at the transmitter, but receives in two polarizations, which means that it gives either HH and HV or VV and VH polarizations. Although some papers have been released using the HH and VV polarization combination[1,51], to the author's knowledge this is a more rare combination, and usually are extracted from a QP sensor. A special case of DP is referred to as CP, which will be further explained in section 3.4.

Last, there is SP SAR, which only measure in one channel. This means that it transmits and receives in just one polarization. SP is however not within the scope of this thesis, and will therefore not be discussed in further detail, but it is still the most used mode for operational (large scale) oil spill detection services.

3.1 Scattering Mechanisms

The behaviour of the backscattered EM radiation depends on several factors, such as properties of the specific sensor, the EM properties of the medium for which the wave propagates in, as well as the EM properties and the geometry of the target. To model the interaction between the incident wave and the observed surface elements, three scattering mechanisms have been defined. These are single-bounce (also known as surface or odd bounce), double-bounce (or even bounce), and volume (or random) scattering[11,18].

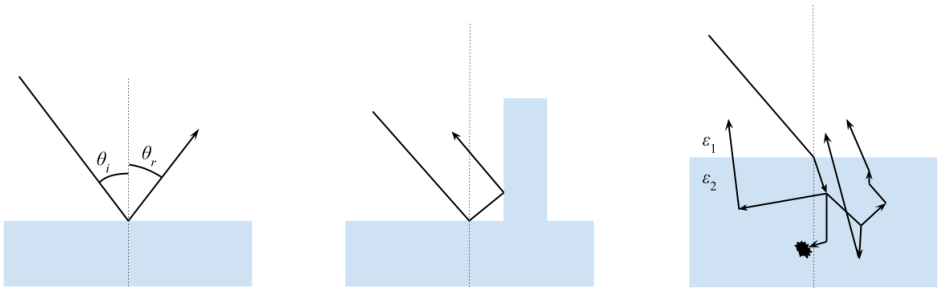

Figure 3.1: Polarimetric scattering mechanisms. The white and blue background colour represents the different media with dielectric constants ϵ_1 and ϵ_2, respectively (e.g. air and water). θ_i is the incident angle and θ_r is the angle of the reflected wave.

3.1.1 Single-Bounce Scattering

When the incident wave hits a slightly rough to polished surface (compared to the incident EM wavelength), the incident wave will bounce off in a clean fashion, as illustrated in figure 3.1a. In the case of an ideal single-bounce backscatter, the incidence angle θ_i equals the reflection angle θ_r. The reflectivity is given by Snell's law, which relates the incident and reflected angle through an refractive index, n, given by Maxwell's relation $n = \sqrt{\epsilon}$, where ϵ is the dielectric constant[6].

The relation between the two media (the white and blue background in figure 3.1a) are related through Snell's law as[11]

$$n_1 \sin(\theta_i) = n_2 \sin(\theta_r) \tag{3.1}$$

Single-bounce is most prominent in the co-pol channels (i.e., HH and VV)[6]. This

is because there is no depolarization of the incidence wave for perfectly smooth surfaces[6]. In other words, the polarization of the incidence wave will be transferred to the reflected wave without alteration, such that both incident and reflected wave will have the same polarization. This also explains why there are no response in the co-pol channels for a perfect single-bounce scatterer.

Examples of single-bounce scattering surfaces are flat surfaces such as smooth ice, calm water. Bragg scattering is a special case of single-bounce scattering, where the variation of the surface height is small compared to the incident wavelength[18].

3.1.2 Double-Bounce Scattering

Double bounce scattering occurs when the incident wave bounces off the surface boundary and into a second reflective surface. Figure 3.1b describes a perfect dihedral double bounce scattering case. As the name suggests, the incident wave is reflected off one surface, then hits a second surface from which it returns to the sensor. For the ideal double-bounce scatterer, only the co-pol channel will receive a response. If the incident wave is horizontally polarized, then the backscattered wave will still be horizontally polarized, but the vertical polarization component of the wave will have gone through a 180 deg shift in phase. For circularly polarized incident waves, the handedness of the signal will shift, i.e. a left-handed incident wave produces a right-handed return wave and vice versa[5].

For oil spill detection, man-made objects tend to create a very strong response due to the double-bounce scattering effect often produced by corners and edges on the structures.

3.1.3 Volume Scattering

Volume scattering occurs when the surface boundary allow some of the incident wave to pass through and scatter within the observed element. Some of the radiated power may be absorbed in the media and dispersed later (as e.g. heat). For a SAR satellite, it does not take a long delay before the reflected signal misses the satellite, as the speed of the satellite is high, and it will move out of the reflection cone relatively quickly. A typical example of volume scattering is the ground being heated by the Sun.[24]

The penetration depth depends on the wavelength of the incident wave, as well as the dielectric properties of the target. In general, longer wavelengths penetrate

deeper than shorter wavelengths, and a large dielectric constant will block most of the transmission into the observed material[11].

3.2 Stokes Parameters

A partially polarized wave (such as SAR backscatter from natural terrain) contains both unpolarized and fully polarized components. The polarization of a partially polarized wave can be fully characterized using a set of real numbers called the Stokes parameters. The combined parameters form the Stokes vector ($\mathbf{S}$) which is defined as[11] [36]:

$$\mathbf{S} = \begin{bmatrix} S_1 \\ S_2 \\ S_3 \\ S_4 \end{bmatrix} = \begin{bmatrix} \langle a_h^2 \rangle + \langle a_v^2 \rangle \\ \langle a_h^2 \rangle - \langle a_v^2 \rangle \\ 2\langle a_h a_v \cos\delta \rangle \\ 2\langle a_h a_v \sin\delta \rangle \end{bmatrix} = \begin{bmatrix} J_{xx} + J_{yy} \\ J_{xx} - J_{yy} \\ 2\Re J_{xy} \\ -2\Im J_{xy} \end{bmatrix} = \begin{bmatrix} S_1 \\ mS_1 \cos 2\chi \cos 2\psi \\ mS_1 \cos 2\chi \sin 2\psi \\ -mS_1 \sin 2\chi \end{bmatrix} \tag{3.2}$$

where $\langle \cdots \rangle$ denotes temporal (or locally spatial) averages. a_h and a_v are the amplitudes of the electric potential vectors orthogonal components, where the subscripts denotes *horizontal* and *vertical* polarization orientation, respectively.

The different J_{pq} terms indicate different elements of the Hermitian positive semi-definite wave covariance matrix, also called the *Wolf* or *Jones coherency matrix*, defined as[18]

$$\begin{aligned} \boldsymbol{J} &= \langle \mathbf{E} \cdot \mathbf{E}^\dagger \rangle \\ &= \begin{bmatrix} \langle E_x^* E_x \rangle & \langle E_x^* E_y \rangle \\ \langle E_y^* E_x \rangle & \langle E_y^* E_y \rangle \end{bmatrix} \\ &= \begin{bmatrix} \langle J_{xx} \rangle & \langle J_{xy} \rangle \\ \langle J_{yx} \rangle & \langle J_{yy} \rangle \end{bmatrix} \\ &= \frac{1}{2} \begin{bmatrix} \langle S_1 \rangle + \langle S_2 \rangle & \langle S_3 \rangle - j\langle S_4 \rangle \\ \langle S_3 \rangle + j\langle S_4 \rangle & \langle S_1 \rangle - \langle S_2 \rangle \end{bmatrix}. \end{aligned} \tag{3.3}$$

† denotes the complex conjugate transpose, * denotes the complex conjugate and j is the imaginary unit.

The last column of equation 3.2 represents the Stokes parameters in terms of the classical Poincaré parameters[36] [49], which are described in chapter 4.3.

The electric potential vector is given as

$$\mathbf{E} = \begin{bmatrix} E_x \\ E_y \end{bmatrix} = \begin{bmatrix} a_h \exp j(\tau + \delta_h) \\ a_v \exp j(\tau + \delta_v) \end{bmatrix}. \tag{3.4}$$

and the following relation is given:

$$S_1^2 = S_2^2 + S_3^2 + S_4^2 \tag{3.5}$$

The Stokes parameters indicate the following different properties of the EM field [18]:

S_1 $\rightarrow$ Total intensity of the wave

S_2 $\rightarrow$ Power of the linear horizontally or vertically polarized components

S_3 $\rightarrow$ Power of the linearly polarized components at tilt angles $\chi = 45°$ or $135°$

S_4 $\rightarrow$ Power in left- and right-handed circularly polarized component of the plane wave

If any of the Stokes parameters has a non-zero value, that indicates the presence of a polarized component in the plane wave [18].
The Stokes vector for the different polarization states can be written as [18]

$$\begin{aligned} S_H &= \begin{bmatrix} 1 \\ 1 \\ 0 \\ 0 \end{bmatrix} \quad S_{RC} = \begin{bmatrix} 1 \\ 0 \\ 0 \\ -1 \end{bmatrix} \\ S_V &= \begin{bmatrix} 1 \\ -1 \\ 0 \\ 0 \end{bmatrix} \quad S_{LC} = \begin{bmatrix} 1 \\ 0 \\ 0 \\ 1 \end{bmatrix} \end{aligned} \tag{3.6}$$

The fact that the Stokes vector can be found merely by reading the power measurements of the backscattered signal, makes this measure especially useful in the case of a non-coherent radar system.
Several useful parameters can be derived from the Stokes parameters. The following sections will describe the derived parameters that are referred to later in this paper.

3.3 Quadrature Polarization

In QP SAR the antenna transmits two orthogonally polarized linear waves in an alternating pattern. The response wave is measured in two orthogonally and linearly polarized channels.

This enables measurements of co- and cross-polarization. The four combinations of transmit and receive polarizations are usually written as a pair of symbols, where H means *horizontal* and V denotes *vertical* polarization, and where the first symbol denotes transmit and the second denotes receive polarization, as described in table 3.1.

Co-polarization	HH	Horizontal transmit, Horizontal receive
	VV	Vertical transmit, Vertical receive
Cross-polarization	HV	Horizontal transmit, Vertical receive
	VH	Vertical transmit, Horizontal receive

Table 3.1: Notation overview for polarimetric combinations on transmit and receive in QP mode.

As a result of utilizing all four polarization channels, it is possible to extract more information about the physical properties of an observed target than what is possible with a single- or dual-pol system. Due to the alternating transmit of Horizontal (H) and Vertical (V) polarization, it is however necessary to either double the length of the antenna or to double the PRF, in order to achieve the same ground coverage as with SP or DP mode. If neither of these options are possible, the ground coverage as a result becomes half or less of what is achievable with the two other mentioned options. In addition, interference between the received echoes can occur, which will disturb the result.[38]

As a note, to avoid interference there is a variant of QP, usually named Quasi-Quadrature Polarization (Quasi-QP), where two DP mode sensors are operated simultaneously. E.g. HH/HV mode is sent at the lower region of the allowable transmit frequency band, while VH/VV is sent in the upper region. As these are operating at different frequencies, they are easily separable, and no interference will occur. Still, the observed HH/HV and VH/VV will be mutually incoherent.

The scattering matrix and scattering vector for QP is defined as

$$\mathbf{\Gamma} = \begin{bmatrix} S_{HH} & S_{HV} \\ S_{VH} & S_{VV} \end{bmatrix} \quad , \quad \boldsymbol{k} = \begin{bmatrix} S_{HH} \\ S_{HV} \\ S_{VH} \\ S_{VV} \end{bmatrix} \tag{3.7}$$

where S_{mn} denotes the elements of the Sinclair scattering matrix[11], and the subscripts mn represent horizontal (H) or vertical (V) transmit and receive polarisation, respectively.

Second order statistics, such as presenting the data as an false-colour composite picture (RGB), will reveal information about the physical properties of the scene. Techniques using one, two or more parameters (i.e. so-called "decompositions"), are also used to further promote specific details, or to enhance more than one type of features. The covariance and the coherency matrices are also part of the second order statistics. For a QP system, the covariance matrix will be the Hermitian outer product of the scattering vector, i.e.[18]

$$C_{QP} = \langle \Omega \Omega^{\dagger} \rangle = \begin{bmatrix} \langle |S_{HH}|^2 \rangle & \langle S_{HH} S_{HV}^* \rangle & \langle S_{HH} S_{VH}^* \rangle & \langle S_{HH} S_{VV}^* \rangle \\ \langle S_{HV} S_{HH}^* \rangle & \langle |S_{HV}|^2 \rangle & \langle S_{HV} S_{VH}^* \rangle & \langle S_{HV} S_{VV}^* \rangle \\ \langle S_{VH} S_{HH}^* \rangle & \langle S_{VH} S_{HV}^* \rangle & \langle |S_{VH}|^2 \rangle & \langle S_{VH} S_{VV}^* \rangle \\ \langle S_{VV} S_{HH}^* \rangle & \langle S_{VV} S_{HH}^* \rangle & \langle S_{VV} S_{VH}^* \rangle & \langle |S_{VV}|^2 \rangle \end{bmatrix} \tag{3.8}$$

where $\langle \cdots \rangle$ denotes spatial ensemble averaging, * denotes the complex conjugate and † denotes the conjugate transpose. For a QP system, all the elements of the covariance matrix are known.

For a monostatic reciprocal target, it is assumed that the Sinclair scattering matrix is symmetrical (i.e. $S_{HV} = S_{VH}$). Consequently, the 4D covariance matrix C_{QP} will reduce to a 3D matrix as

$$C_{QP}^{reciprocity} = \langle \Omega \Omega^{\dagger} \rangle = \begin{bmatrix} \langle |S_{HH}|^2 \rangle & \sqrt{2} \langle S_{HH} S_{HV}^* \rangle & S_{HH} S_{VV}^* \\ \sqrt{2} \langle S_{HV} S_{HH}^* & 2 \langle |S_{HV}|^2 \rangle & \sqrt{2} \langle S_{HV} S_{VV}^* \rangle \\ \langle S_{VV} S_{HH}^* \rangle & \sqrt{2} \langle S_{VV} S_{HV}^* \rangle & \langle |S_{VV}|^2 \rangle \end{bmatrix} \tag{3.9}$$

Reciprocity is often used as an assumption to simplify the expressions in e.g. decompositions.

Another technique that is often used, are transformations of the scattering vector $\mathbf{s}$, i.e. changing the basis sets. An example of such a transformation is the Pauli

basis, which gives the 4D Pauli vector defined as[18]

$$\mathbf{s} = \frac{1}{\sqrt{2}} \begin{bmatrix} S_{HH} + S_{VV} \\ S_{HH} - S_{VV} \\ S_{HV} + S_{VH} \\ j(S_{HV} - S_{VH}) \end{bmatrix} \tag{3.10}$$

where the elements S_{ij} are linear combinations of the Sinclair scattering matrix. The coherency matrix is then generated by taking the Hermitian outer product of the Pauli vector. Similarly to the Covariance matrix above, if assuming reciprocity, the Pauli vector is reduced to 3D due to the symmetry constraint[18]

$$\mathbf{s} = \frac{1}{\sqrt{2}} \begin{bmatrix} S_{HH} + S_{VV} \\ S_{HH} - S_{VV} \\ 2S_{HV} \end{bmatrix} \tag{3.11}$$

3.4 Hybrid Polarization

The HP mode was introduced by Raney[35]. Raney also holds the patent for the HP method and architecture for obtaining the Stokes parameters from radar backscatter[33]. The patented architecture is described in figure 3.2.

In HP mode the *transmission* is done using circular polarization, while *receiving* two orthogonal mutually coherent linear polarizations. The benefit of transmitting circular polarization is that the problem with the small swath size of QP is eliminated, as transmission is done across all polarizations at once. Consequently, there is no need to increase the PRF (ref. chapter 3.3). In addition, HP gives a radar system which is relatively simple to implement compared to a QP radar. It also has low susceptibility to noise and cross-channel errors, and rather unique self-calibrating features.[35]

If the relative phase between the received polarization is maintained, the linear orientation does not matter.

Circular polarization ratio expressed in terms of the Stokes parameters:

$$(S_1 - S_4)/(S_1 + S_4) \tag{3.12}$$

As the access to real HP data was (naturally) non-existing at the time that the

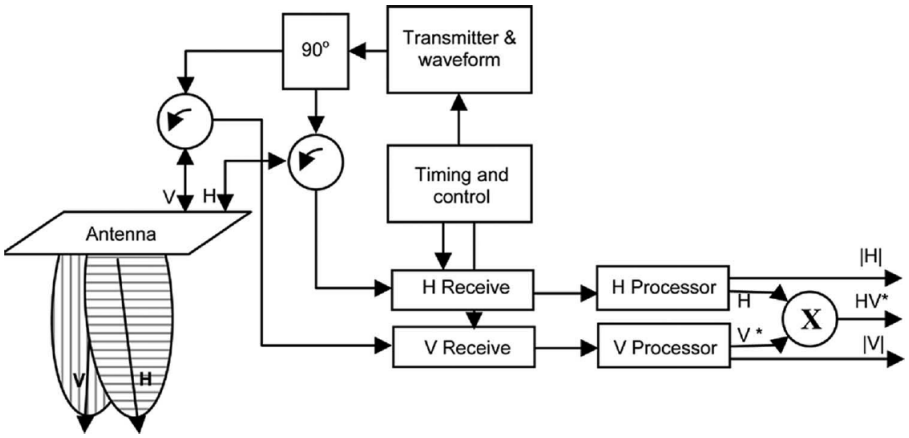

Figure 3.2: Raney's architecture for generic hybrid polarization SAR, for which the transmitted field is circularly polarized and the receive dual-polarization basis is linear (Illustration from Raney[35])

mode was suggested, a transformation process from QP data was suggested, which describes how to simulate the Stokes vector, **S**. This process consists of 5 steps:

Step 1) Evaluate the electric vector $\boldsymbol{E_B}$ of the backscattered field generated by right-circular illumination $\boldsymbol{R}$ impinging upon a scene described by the 2×2 Sinclair Matrix:

$$\boldsymbol{E_B} = [\Gamma]\boldsymbol{R} \tag{3.13}$$

where

$$\boldsymbol{R} = \frac{1}{\sqrt{2}}[1 - j]^{\boldsymbol{T}} = \frac{1}{\sqrt{2}}\begin{bmatrix} S_{xx} - jS_{xy} & S_{xy} - jS_{yy} \end{bmatrix}^{\boldsymbol{T}} \tag{3.14}$$

and S_{ij} are the elements of $[\Gamma]$.

Step 2) Derive the corresponding $\boldsymbol{E_H}$ and $\boldsymbol{E_V}$ vectors of the Single-Look Complex (SLC) image observe through a linearly dual-polarized (H and V) antenna, receiver and processor sequence:

$$\begin{aligned} \boldsymbol{E_H} &= \begin{bmatrix} 1 & 0 \end{bmatrix} E_{\boldsymbol{B}} = \frac{1}{\sqrt{2}}(S_{xx} - jS_{xy}) \\ \boldsymbol{E_V} &= \begin{bmatrix} 0 & 1 \end{bmatrix} E_{\boldsymbol{B}} = \frac{1}{\sqrt{2}}(S_{xy} - jS_{yy}) \end{aligned} \tag{3.15}$$

Step 3) Evaluate the four elements of the coherency matrix $\boldsymbol{J}$ (3.2):

$$\begin{aligned} 2J_{xx} &= \langle|S_{xx}|^2\rangle + \langle|S_{xy}|^2\rangle + j\langle S_{xx}S_{xy}^*\rangle - j\langle S_{xy}S_{xx}^*\rangle \\ 2J_{xy} &= \langle S_{xx}S_{xy}^*\rangle - \langle S_{xy}S_{yy}^*\rangle - j\langle|S_{xy}|^2\rangle - j\langle S_{xx}S_{yy}^*\rangle \\ J_{yx} &= J_{xy}^* \\ 2J_{yy} &= \langle|S_{yy}|^2\rangle + \langle|S_{xy}|^2\rangle - j\langle S_{yy}S_{xy}^*\rangle + j\langle S_{xy}S_{yy}^*\rangle \end{aligned} \tag{3.16}$$

Step 4) Evaluate the Stokes vector $\mathbf{S}$ from the elements of $\boldsymbol{J}$:

$$\begin{aligned} S_1 &= J_{xx} + J_{yy} \\ S_2 &= J_{xx} - J_{yy} \\ S_3 &= \Re\{\langle S_{xx}S_{xy}^*\rangle + \langle S_{xy}S_{yy}^*\rangle\} - \Im\langle S_{xx}S_{yy}^*\rangle \\ S_4 &= -\Im\{\langle S_{xx}S_{xy}^*\rangle - \langle S_{xy}S_{yy}^*\rangle\} - \Re\langle S_{xx}S_{yy}\rangle + \langle|S_{xy}|^2\rangle \end{aligned} \tag{3.17}$$

Step 5) Last, evaluate the Stokes parameters by substituting corresponding data array elements from the $\boldsymbol{C_3}$ covariance matrix of the original QP data:

$$\begin{aligned} S_1 &= \frac{1}{2}(C_{11} + C_{22} + C_{33}) \pm \frac{1}{\sqrt{2}}(\Im C_{12} + \Im C_{23}) \\ S_2 &= \frac{1}{2}(C_{11} - C_{33}) \pm \frac{1}{\sqrt{2}}\Im C_{12} \mp \frac{1}{\sqrt{2}}\Im C_{23} \\ S_3 &= \frac{1}{\sqrt{2}}(\Re C_{12} + \Re C_{23}) \pm \Im C_{13} \\ S_4 &= \frac{1}{\sqrt{2}}(-\Im C_{12} - \Im C_{23}) \mp \Re C_{13} \pm \frac{1}{2}C_{22} \end{aligned} \tag{3.18}$$

Note that the upper and lower signs of the $\pm$ and $\mp$ in step 5) represents left circular transmit, linear receive (LCTLR), and right circular transmit, linear receive (RCTLR), respectively[20].

Chapter 4

Polarimetric Parameters for Oil Spill Detection on Sea Water

In this chapter, parameters that have previously been considered for oil spill detection and/or characterization, will be described. How promising the parameter appear to be, as well as how often it occurs in existing literature, have been two of the major considerations in the process of selecting parameters to consider in this Thesis.

Parameters used for detecting and/or characterizing oil spills on sea water using HP SAR data, has been listed in table 4.1. This table also shows which parameters that are covered in this thesis.

Table 4.1: List of various HP parameters used for oil spill detection. The chapters for the parameters that has been evaluated in this thesis is given in the rightmost column.

Parameter	**Symbol**	**Evaluated in chapter**
The Stokes Parameters	S_1, S_2, S_3 and S_4	6.3
The Degree of Polarization	m	6.4
The Degree of Depolarization	$\overline{m}$	
The Degree of Linear Polarization	m_L	
The Degree of Circular Polarization	m_C	
The Circular Polarization Ratio	μ_C	
The Linear Polarization Ratio	μ_L	
The Orientation of Effective Polarization Ellipse	ψ	
The Axial Ratio of the Polarization Ellipse	r	
The Poincaré Ellipticity Parameter	χ	6.5
Entropy	H	6.7
$m-\chi$ Decomposition	$m-\chi$	6.6

4.1 The Stokes Parameters

As described in chapter 3.2, the Stokes parameters characterizes the polarization of a partially polarized wave. The Stokes parameters form the basis for several HP parameters, which will be further detailed in the following sections. The fact that it is possible to extract the Stokes parameters without further processing, such as e.g. reconstruction of the QP covariance matrix, makes for quick processing of the HP parameters which are based on Stokes parameters.

In addition to this, the four Stokes parameters individually represent different properties of the EM field. As a result of this, they will without further processing enhance their respective elements of the EM backscatter. In spite of this, to the knowledge of the author, the bulk of the performed studies consider parameters or decomposition techniques based on the Stokes parameters, rather than utilizing the individual analytical power of the separate Stokes parameters themselves.

S_1 represent the total intensity of the backscattered wave, and is thus quite similar to oil spill detection based on the total power of the four polarimetric channels in QP systems[25]. S_2 represent the power of the linear horizontally or vertically polarized components, which are the channels that is used for receiving HP data. S_3 give the power of the linearly polarized components at tilt angles $\chi = 45\,\text{deg}$ or $135\,\text{deg}$, while S_4 correspond to the power in the left- and the right-handed circularly polarized component of the plane wave (see chapter 3.2).

Li et al.[21] conducted an investigation into the capacity of S_2 for oil spill detection with HP SAR, simulated from RADAR Satellite 2 (RADARSAT-2) fine QP SAR. Li et al.[21] utilizes the Otsu threshold analysis[30] to threshold the backscattered response for S_2. The Otsu threshold is a relatively simple and well-known method, using the bi-modal structure of the histogram, in this case, the histogram for S_2. Li et al.[21] demonstrated that this method is effective on separating different oil types from clean sea surface. Their conclusion is that their proposed method potentially can provide auto-detection of oil slicks over large coverage areas, within an optimal incidence angle range of $20\,\text{deg} - 45\,\text{deg}$ and wind speeds between $3 - 10m/s$.

No noise analysis was performed on the data sets evaluated by Li et al.[21], but they mention that a moving window averaging method with a window size of 10x10 pixels was used to reduce speckle noise.

4.2 The Degree of Polarization

The DoP is defined as the relative intensity of the polarized component to the intensity of the total field, and is a parameter easily derived from the Stokes parameters. In mathematical terms, it is expressed as [34,35]

$$m = \frac{\sqrt{S_2^2 + S_3^2 + S_4^2}}{S_1} = \sqrt{1 - 4\frac{|\mathbf{J}|}{\mathrm{Tr}(\mathbf{J})}} \qquad 0 \leq m \leq 1; \tag{4.1}$$

where S_{1-4} represents the different Stokes parameters, and $\boldsymbol{J}$ is the wave covariance matrix (3.3). The $\mathrm{Tr}(\mathbf{J})$ is the trace of $\mathbf{J}$ and represents the total energy of the wave. $m = 0$ indicates a fully depolarized wave and $m = 1$ indicates a fully polarized wave. Any values between 0 and 1 indicate the percentage of polarization in the partially polarized wave.

The DoP has been considered in a number of articles already, and has in general been deemed an interesting and effective parameter for oil slick detection. Its computationally efficient estimation is often accentuated as one of its main advantages [36,43]. It is also rather common to test the DoP as part of a decomposition with one or more additional parameters, such as e.g. in the $m - \chi$ decomposition which is tested and evaluated in chapter 6.6. The literature regarding this decomposition will be discussed in chapter 4.4. Other decompositions have not been included in this thesis.

The first to suggest the DoP as a method for detecting oil slicks on sea water using HP SAR data, was Shirvany et al. [43]. By comparing the DoP calculated from both QP VH-VV and HH-VV, as well as calculated from HP and $\pi/4$ data, they concluded based on their findings that HP data was at least as sensitive to oil slicks as QP data. They also found that the edges and structures within the oil slick itself was distinguishable using the DoP on HP data.

Li et al. [20] analyses the performance of the DoP with simulated HP data, based on RADARSAT-2 and UAVSAR QP SAR data. In the UAVSAR images, which has a quite wide incidence angle range stretching from 22 deg to 65 deg, they find that the DoP value slowly decreases as the incidence angle increases. With the two RADARSAT-2 scenes, they find that the difference between oil-covered and clean sea is larger in the scene with the steeper incidence angle. They also find that the DoP is able to reveal oil structures and properties, supporting what Shirvany et al. [43] found.

Similar characteristics were also found by Yin et al.[52]. The DoP shows internal variations in the backscattered intensity within the oil slick, however they find that it also is very responsive to LWR. They also consider an Oleyl Alcohol (OLA) slick as a look-alike feature. This is effectively dampened by the DoP, although it is still barely visible. Their findings indicate that the DoP is not effective distinguishing between double- and single-bounce scattering, as both ships (double-bounce scattering) and the sea surface (Bragg scattering) exhibit high values of DoP. Additionally, for the scenes they consider, the values for DoP for most sea surfaces, oil-spills and ships are above 0.5, indicating that the sole use of DoP as a discriminator have limited capabilities.

Salberg et al.[40] used the DoP for comparison when suggesting their Coh measure. They also evaluated the conformity index, the ellipticity parameter, the ρ_{CL} measure and the standard deviation of the Co-polarized Phase Difference (CPD). For all their considered images, the DoP performed similarly to the conformity index and the ρ_{CL} measure. Although it was not their primary field of investigation, it appears that the DoP performed well on distinguishing oil from sea, but not too well distinguishing between look-alikes and oil.

Nunziata et al.[29] consider two scenes from Advanced Land Observation Satellite, aka DAICHI (ALOS) and two scenes recorded by RADARSAT-2. They evaluate the squared modulus VV-polarized image, the entropy, the $\mu_{\mathbf{C}}$, the $|\mu_{hv}|$, the $|\delta_{hv}$ and the $|\sigma_{hv}|$ as well as the DoP. They find that the DoP has a higher value within the slick-covered areas than over clean sea, indicating that the Bragg/tilted-Bragg scattering applies for all areas but the slick-covered. I.e., close to unpolarized waves are backscattered from the oil-covered areas, while nearly fully polarized waves are scattered from everywhere else. The DoP is also able to distinguish between different scattering characteristics within the area which in the VV-polarized intensity image appear to be nearly uniformly dark. In the DoP image, this dark area is clearly divided between the actual oil slick covered water (which is accentuated) and what is probably caused by low wind in the same area (which is significantly dampened).

4.2.1 Parameters closely related to the Degree of Polarization

Depolarization is associated with a reduction in the DoP of incident states[43], and the Degree of Depolarization (DoD) is defined as $1-m$. The DoD indicates random backscatter, which typically comes from semi-transparent volumetric material such as e.g. forest canopy[36].

Also related to the DoP, and possible to calculate directly from the Stokes parameters, are the Degree of linear polarization (DoP_l), $m_{\mathbf{L}}$

$$m_{\mathbf{L}} = \frac{\sqrt{S_2^2 + S_3^2}}{S_1} \tag{4.2}$$

the Degree of circular polarization (DoP_c), $m_{\mathbf{C}}$

$$m_{\mathbf{C}} = \frac{S_4}{S_1} \tag{4.3}$$

the Circular Polarization Ratio (CPR), $\mu_{\mathbf{C}}$

$$\mu_{\mathbf{C}} = \frac{S_1 - S_4}{S_1 + S_4} = \frac{J_{hh} + J_{vv} - 2\Im J_{hv}}{J_{hh} + J_{vv} + 2\Im J_{hv}} \tag{4.4}$$

the linear polarization ratio (LPR), $\mu_{\mathbf{L}}$

$$\mu_{\mathbf{L}} = \frac{S_1 - S_2}{S_1 + S_2} \tag{4.5}$$

the orientation of the effective polarization ellipse, ψ

$$\psi = \frac{1}{2} tan^{-1}\left(\frac{S_3}{S_2}\right) \tag{4.6}$$

and the axial ratio of the polarization ellipse, r, given by

$$r = tan\left[\frac{1}{2} sin^{-1}\left(\frac{S_4}{mS_1}\right)\right] \tag{4.7}$$

The ψ and the r are in combination with the power of the electric field, P_e, sufficient to fully describe the ellipse formed by the electric vector $\mathbf{E}$ of a polarized wave.

4.3 The Poincaré Ellipticity Parameter

The ellipticity parameter is commonly referred to as χ. In the literature, as found in the pilot study for this thesis, the χ is one of the parameters showing potential in detecting and potentially partially characterising oil spills on sea water [20,40,52]. The χ indicates the sign of rotation of the ellipse, as well as its ellipticity, and is one of the Poincaré variables (ψ, χ and m) derived from the Stokes parameters. The sign of χ is an unambiguous indicator of odd versus even bounce backscatter, even if the radiated EM field is not perfectly circularly polarized [36]. Together with the DoP and the ψ, the Poincaré ellipticity parameter is sufficient to describe the polarized portion of a partially polarized EM field (see figure 4.1).

The doubled ellipticity (2χ) and orientation (2ψ) parameters represents the EM wave's longitude and latitude.

The χ may be represented as a measure for the Degree of Circularity (DoC), defined as:

$$\sin(2\chi) = -\left(\frac{S_4}{mS_1}\right) \qquad -\frac{\pi}{2} \leq \chi \leq \frac{\pi}{2} \tag{4.8}$$

It is easily seen that this is derived from the expression for S_4 in equation 3.2.

The χ has also often been used in conjunction with the DoP [14–16], a combination often referred to as the $m - \chi$ (see section 4.4).

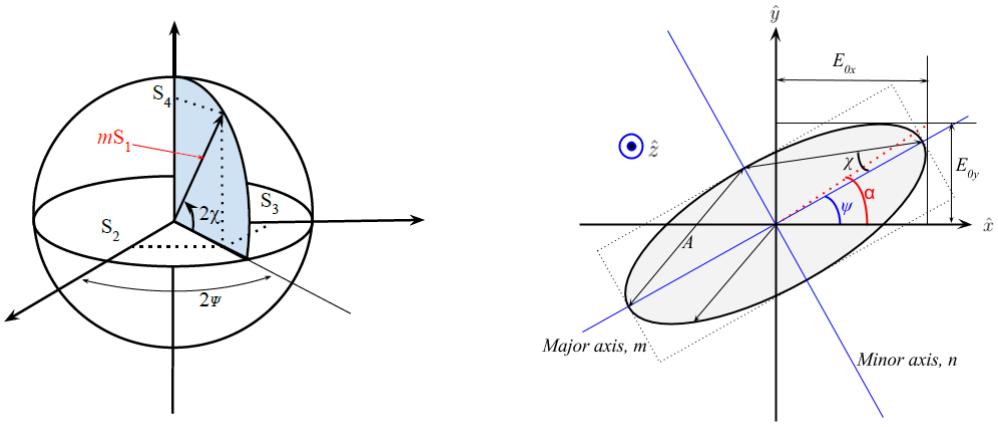

(a) (b)

Figure 4.1: The Poincaré Sphere (a) and the Polarization ellipse (b)

Li et al.[20] found a reversal of signs for χ when they compared clean sea with natural seeps in the Mexican Gulf. Clean sea showed negative values, while oil-covered water had a positive response. The same behaviour was however not observed when they compared clean sea to oil from the Deep Water Horizon (DWH) oil spill. Li et al.[20] suggests that the sign reversal could be due to the different types of oil considered, i.e. that one is a natural seep and the other a man-made oil spill. However, it could be argued that these are not in fact that different, as both the natural seep and the DWH are released from the sea bed, and the oil have to travel through the depth of the water. In that respect, the oil from the DWH accident, although *caused* by human activity and not just naturally leaking from the sea bed, is also a seep. Still, there are some differences, which includes the depth of the point of release (the DWH release happened at approx. 1.500 meters[39]) and thus the length of the transport to the surface, the local sea currents which may alter the length of transport and also disperse and dilute the oil as it travels to the surface, concentration at the point of release, the rate of flow, and of course, the sheer volume of the release (by 15 July 2010, when the oil well was finally capped and sealed after 87 days of leakage, an estimated massive 206 million gallons (4.9 million barrels) had been released[32]). In this respect, the DWH is quite different from what is often considered an oil spill, and more similar to the natural seep, as we often think of a spill as something which is released onto the surface from above, or at least close to the surface (e.g. from a ship or similar). It is likely that a release from the sea bed is much more diluted and dispersed when it reaches the sea surface, than if the release was done at or above the surface, so this should be taken into account for this comparison.

Li et al.[20] used HP data simulated from RADARSAT-2 SLC fine QP data when observing the sign reversal, as well as to cover the DWH oil spill. The noise floor for the RADARSAT-2 data is given as < -35 dB, which is much lower than for RISAT-1, which is -16.8 dB. Looking at the colorbars in figure 1 in the article by Li et al.[20], it appear that the values within the considered scenes run from approximately -35 to -20 for the first scene (a), and from approximately -30 to 0 in the second scene. Looking merely at these figures for the two RADARSAT-2 images, it looks like the oil slick in the first scene is very close to the noise floor, while the second is not so close. This could suggest that the χ is in fact affected by the noise in the first image.

Salberg et al.[40] also considered the χ as part of their article, using HP data simulated from QP RADARSAT-2 data. In total, they considered 5 scenes. The first scene covered the Oil on Water (OoW) exercise in 2012, while the second scene covered OoW exercise in 2012, then two scenes covered the DWH accident, before finally the fifth scene covered again the OoW in 2011, but this time the scene just

captured a LWR, not any oil slicks.

Salberg et al.[40] found that the performance of the χ varied much more than the other parameters they considered (Coh, VV, μ, DoP, σ_{CPD}, ρ_{CL} and a combination of the Coh, the DoP and the μ). The scenes considered by Salberg et al.[40] appear to give a different response to oil slicks at an incidence angle below $35 - 38$ than above. For slicks below this limit, the response is a bright colour compared to the clean sea, while for slicks above this limit the response is a dark colour compared to the clean sea. The authors state that the reason for the variable result is unclear, although they suggest that the reason may be related to the Bragg scattering assumption, wind speed, incident angle, oil type or oil spill thickness. The colour change could however resemble the sign reversal observed by Li et al.[20]. This will be discussed further in chapter 6.5.

Yin et al.[52] found that the χ did perform relatively poorly both for oil and for ship detection, although it was possible to use it. However, they did find that it added value to the DoP when used as part of the $m - \chi$ decomposition. χ alone could not separate OLA from the clean sea surface, but if detecting *oil* is the only goal, it may be claimed that this is a good thing. The authors conclude that the χ is not sensitive to surface slicks, although it is sensitive to ships and it does perform better than δ on oil detection. Their opinion is that using single parameters makes it difficult to discriminate oil-spills (and ships) from the sea surface, and that combinations should be used to increase the odds for successful detections. The analysis was performed on HP SAR simulated from QP RADARSAT-2 and SIR-C/X-SAR data.

Yin et al.[52] used both RADARSAT-2 and Spaceborne Imaging Radar-C/X-band Synthetic Aperture Radar (SIR-C/X-SAR) data to evaluate χ (amongst several other parameters). Their results are a bit contradictory, as the text states that the parameter is "valid" for RADARSAT-2, but unsatisfactory for SIR-C/X-SAR, while the illustration (see Yin et al.[52], figure 8) seem to suggest that χ give a noticeable response for oil spills using SIR-C/X-SAR and for LWR using RADARSAT-2, but suppresses OLA using SIR-C/X-SAR and oil spills using RADARSAT-2. So, the illustrations suggest that there is a benefit using χ for SIR-C/X-SAR, while it is not usable for RADARSAT-2, but the text states the opposite. Of course, the quality of the figures in the article may not be good enough to fully assess the results by visual inspection, as they have been resized to fit 4 images in one line across the page in the article.

Using histograms to further evaluate the separability in the SIR-C/X-SAR scenes, Yin et al.[52] find that the χ is unable to separate OLA from clean sea, but it is able to separate oil spills from the clean sea. However, the histogram is based

on two different scenes, which although they were produced by the same satellite, have very different incidence angle ranges, and which are recorded 8 days apart. The incidence angle range for the two RADARSAT-2 and the two SIR-C/X-SAR scenes considered by Yin et al.[52] are shown in figure 6.6, as (d), (e), (f) and (g), respectively. It is seen that both the two RADARSAT-2 scenes and the two SIR-C/X-SAR scenes are separated by quite a long distance with regards to incidence angles. This will affect the backscattered signal, and the fact that the scenes are recorded many days apart, opens the possibility for dramatic weather condition changes, which is not detailed in the article.

The noise floor for the respective satellites is not given in the article by Yin et al.[52], nor is the signal to noise ratio (SNR), and no noise analysis is included in the text. This would have been useful in order to evaluate the quality of the received signal, and to see if it is likely that the signal is corrupted by noise.

4.4 The m-χ Decomposition

The $m-\chi$ decomposition ($m-\chi$) was first suggested for HP by Raney et al.[36] as a method to describe lunar craters, using imagery from the MiniRF instrument on-board NASA's LRO. It has later been considered also for oil spill characterization by several articles[14–16,52].

Raney et al.[36] proposes a method of visualizing the $m-\chi$ decomposition through a color-coded RGB image, where

$$\begin{aligned} R &= \left[\frac{m * S_1(1+\sin 2\chi)}{2}\right]^{1/2} \\ G &= [S_1(1-m)]^{1/2} \\ B &= \left[\frac{m * S_1(1-\sin 2\chi)}{2}\right]^{1/2} \end{aligned} \tag{4.9}$$

In this form, the blue channel indicate single-bounce (and Bragg) backscatter, red corresponds to double-bounce, while the green channel indicate the randomly polarized constituent[36].

As seen, the entire decomposition is based upon various combinations of the Stokes parameters, and is therefore not dependent on preprocessing such as reconstruction.

Yin et al.[52] considered the $m-\chi$ as part of their article. As noted in chapter 4.3, the article does not state weather conditions, SNR or the noise equivalent sigma zero (NESZ), and it appears that the distinction between oil and clean sea, as well as the distinction between the lookalike OLA is based upon two different scenes, although the result is presented in one graph.

The presented results indicate that the χ improves the result by 4.6% and 3.9% for oil and OLA, respectively, compared to the results the authors achieved by using the $m-\delta$ decomposition ($m-\delta$), which was also considered. They do however conclude with the extended Bragg (X-Bragg) method that they present being even more accurate in the distinction of oil vs OLA vs clean sea.

Jayasri et al.[14] state that the χ is effective in characterizing oil spills on sea water. However, their presented results is only considering the $m-\chi$ decomposition, so it is unclear if they have in fact tested the χ alone. The authors also note that the distinction between slick types become more pronounced by increasing incidence angle, similar to some of the articles considering the χ[20,40].

Jayasri et al.[14] have used actual HP data acquired by RISAT-1, in contrast to most other articles on HP SAR, which use HP data simulated from FP SAR sensors. They find that "the mean backscattering coefficient over oil-covered water and over clean sea is 4.6 dB and 3.55 dB above the NESZ in the RV and RH channels, respectively"[14]. When reducing specle noise using a gamma filter on SLC HP SAR data, they find that the standard deviation is less than one standard deviation above the NESZ. The significance of this to the results of this thesis, is discussed in chapter 6.6.

The $m-\chi$ is also considered in the articles by Kumar et al.[15] and Kumar et al.[16]. These are both written by the same authors, approximately one year apart. The articles are more or less similar, although the latter is more elaborate and includes also $m-\psi$ decomposition ($m-\psi$) and $m-\alpha$ decomposition ($m-\alpha$). However, the same article does not include information about what the considered lookalikes are. Although it is still not specifically stated in the first article, at least this tells us that the lookalikes are recorded somewhere in near the Gulf of Mexico, and not (as it may appear) as part of the OoW exercise 2012, which is when and where the scene containing the oil spill is recorded. It would have been useful with more in situ data for these scenes, as well as a clear statement as to what the lookalike is.

From the results presented in the articles Kumar et al.[15] and Kumar et al.[16], it actually may seem like the $m-\chi$ is more sensitive to the lookalike (whatever that is) than it is to the oil emulsion. However, important data such as the incident angle, wind/weather conditions, time between oil discharge and recording of the

SAR image, oil properties, and what the lookalike is, is omitted in both articles. There is a vague hint that there may be some time between the discharge of the oil and the recording in the first article, but no precise time for either is given. This unfortunately makes it harder to evaluate the presented results with any accuracy. However, both articles conclude that the $m-\chi$ is usable for distinguishing oil from lookalikes as well as both of these from clean sea.

4.5 The Entropy

The H is a measure for target disorder[49]. The definition for coherent DP data is based upon the eigenvalues given by Raney[35] as

$$\lambda_{1,2} = \frac{1}{2}(1 \pm m) \quad \text{where } \lambda_1 + \lambda_2 = 1 \quad \text{and } 0 \leq m \leq 1 \tag{4.10}$$

Raney[35] also gives the expression for the entropy as

$$H = -\sum_{i=1}^{2} \lambda_i \ln \lambda_i \tag{4.11}$$

and states that the entropy should be zero when $\lambda_1 = 1$, and have the maximum value of unity when $\lambda_1 = \lambda_2 = 1/2$. These extremes corresponds to when $m = 1$ and when $m = 0$, respectively, or in other words to the fully polarized and the fully depolarized case.[35]

However, there is a problem with equation 4.11, as it does not give $H = 1$ when $m = 0$, but $H = \ln 2$. Comparing the equation with other sources, such as Lee and Pottier[18] (although they give the H for QP systems), and then doing the calculations, it seems likely that the following expression is correct according to the given extreme values

$$H = -\sum_{i=1}^{2} \lambda_i \log_2 \lambda_i \tag{4.12}$$

That is, using the logarithm with base 2, and not the natural logarithm. This also corresponds with the general definition for the Entropy[18,49]. When using base 2, the correct extreme values are achieved (which also is natural, given that these are 2D data). Therefore, equation 4.12 has been used for calculating the entropy in this thesis.

The H, although previously considered for oil slick analysis using QP data, has

just recently been considered for HP data. Last year, Nunziata et al. [29] evaluated the performance of the H for oil slick analysis. The study used data recorded by ALOS and RADARSAT-2, but did not have access to actual HP data. Thus, the results were based on HP data simulated from QP data.

Nunziata et al. [29] also discuss the NESZ and the impact the noise has on the results to some degree. In one scene, they find that noisy pixels are contained within the oil covered area.

Chapter 5

Data Sets

An overview of the data sets considered in this thesis are found in table 5.1. These scenes are chosen as they are among the few available RISAT-1 FRS-1 images with good in situ data, and covering confirmed oil slicks. The scenes also have overlapping FP RADARSAT-2 data from approximately the same time, although this thesis does not consider these. In situ data makes for extra information not available from the SAR data, and the overlapping RADARSAT-2 data gives possibilities for future comparison with FP data.

Table 5.1: List of scenes considered in this thesis

	#1	#2
Sensor	RISAT-1	RISAT-1
Acq. Date	30-05-15	10-06-15
Imaging Time (UTC)	12:05:51	07:19:18
Incident angle	34.47183°	44.02802°
Wind Speed	... m/s	12 $^m/_s$
Wind Direction	...°	263.2°
Features	Natural seep, man-made objects	Oseberg Blend emulsion, Plant oil (Radiagreen), Oil emulsion

5.1 Scene 1

The scene was recorded on May 30, 2015, over the Cantarel seep in the Mexican Gulf. The Cantarel is a known seep often used to test oil spill detection methods, as it is relatively constant and therefore predictable. The full scene can be viewed in figure 5.1.

Figure 5.1: Scene 1, full scene. The red square shows the sub-scene used for calculations. Unless otherwise stated, references to scene 1 are referring to the subscene (also seen in figure 5.2). RISAT-1

Unfortunately, wind information for this scene has not been found.

In this particular scene, there are multiple man-made objects (oil installations). There are also some alleged wind shadows formed behind the installations. A weak wave pattern is also visible moving diagonally across the image. The contrast is still good between the clean sea and the oil seep. To enhance the dynamic range in the analysis of the various parameters, the man-made objects have been masked out before applying the parameters, by a threshold value. This did also remove some of the most intense salt noise (high intensity speckle).

For calculations, a segment has been extracted and used, focusing on the area surrounding the oil seep. The extracted segment is outlined in figure 5.1. No smoothing was done during the extraction of the sub-scene.

The extracted segment is shown in figure 5.2. In this figure, the rectangular shapes represent areas used for calculating mean and standard deviation for different features. The red rectangles represent the oil seep, the blue rectangles represent clean sea, and the green rectangle is an example of alleged wind shadow.

For the remainder of this thesis, the extracted subset is what is referred to by scene 1.

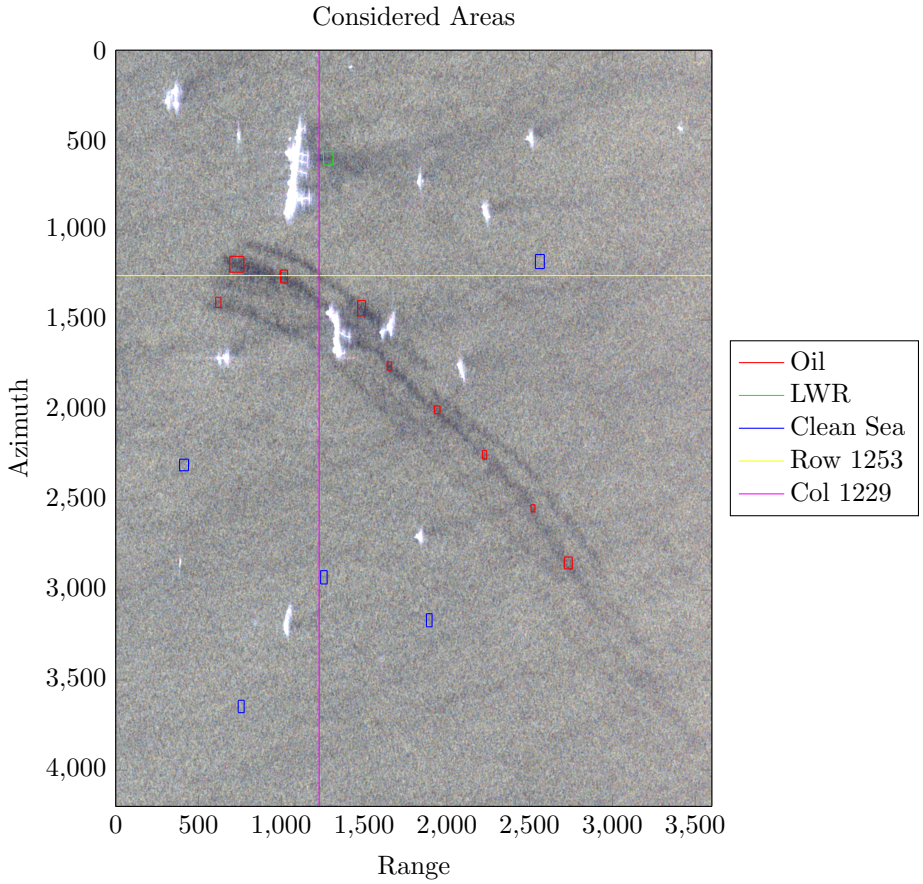

Figure 5.2: Sub-scene of scene 1 (4201 × 3601 pixels). Areas used for calculations are given as red (Oil Seep), green (suspected Wind Shadow) or blue (Clean Sea) rectangles. The yellow and pink line are used for observing value change across the image features. RISAT-1 ©2015-Antrix, processed by KSAT, all rights reserved 2015

Table 5.2: Scene 1, metadata

Satellite	RISAT-1
Processing station	KSAT
Imaging date	30 May 2015
Product ID	1513311005
Scene start time	12:05:51.110 UTC
Scene center time	12:05:53.311 UTC
Scene end time	12:05:55.611 UTC
Imaging orbit number	17034
Processing Level	SLC
Imaging mode	FRS-1
Polarization	RH + RV
Sensor orientation	Left
Orbit node	Descending
Incidence angle	34.47183°
Satellite altitude	540.736 km
Line spacing	2.09
Pixel spacing	1.80
Noise equivalent sigma zero (NESZ)	−16.7999992
Calibration Constant γ_0, RV	67.176
Calibration Constant γ_0, RH	70.321
Calibration Constant β_0, RV	65.545
Calibration Constant β_0, RH	68.690

5.2 Scene 2

The scene shown in full size in figure 5.3, was recorded on June 10, 2015 as part of the Oil on Water (OoW) exercise. The scene cover 6 verified slicks of different types and concentrations, as detailed in table 5.3. The slicks were discharged over a period of two successive days, on 9 June and 10 June, respectively. For this thesis, only the slicks from 10 June has been evaluated (i.e. slicks C, D, E and F), as these appear to give a slightly better contrast to the surrounding clean sea. The subset is shown in figure 5.4. In the coming chapters, this subset will be referred to as Scene 2.

The OoW exercise is an annual event organized by Norwegian Clean Seas Association for Operating Companies (NOFO), that takes place at the Frigg field in the North Sea. The exercise is a large-scale operation involving representatives

Table 5.3: Slick details for scene 2. The slick # corresponds to the letters in figure 5.3.

Slick #	**Discharge Date/Time**	**Slick type**	**Amount**
A	June 9, 06:45	Oseberg Blend emulsion, 65 % water (OB65)	$45m^3$
B	June 9, 12:30	Oseberg Blend emulsion, 65 % water (OB65)	$35m^3$
C	June 10, 04:48	Plant oil (Radiagreen)	$0.2m^3$
D	June 10, 04:59	Oil emulsion, 60 % water (EM60)	$0.5m^3$
E	June 10, 05:15	Oil emulsion, 40 % water (EM40)	$0.5m^3$
F	June 10, 05:30	Oil emulsion, 20 % water (EM20)	$0.5m^3$

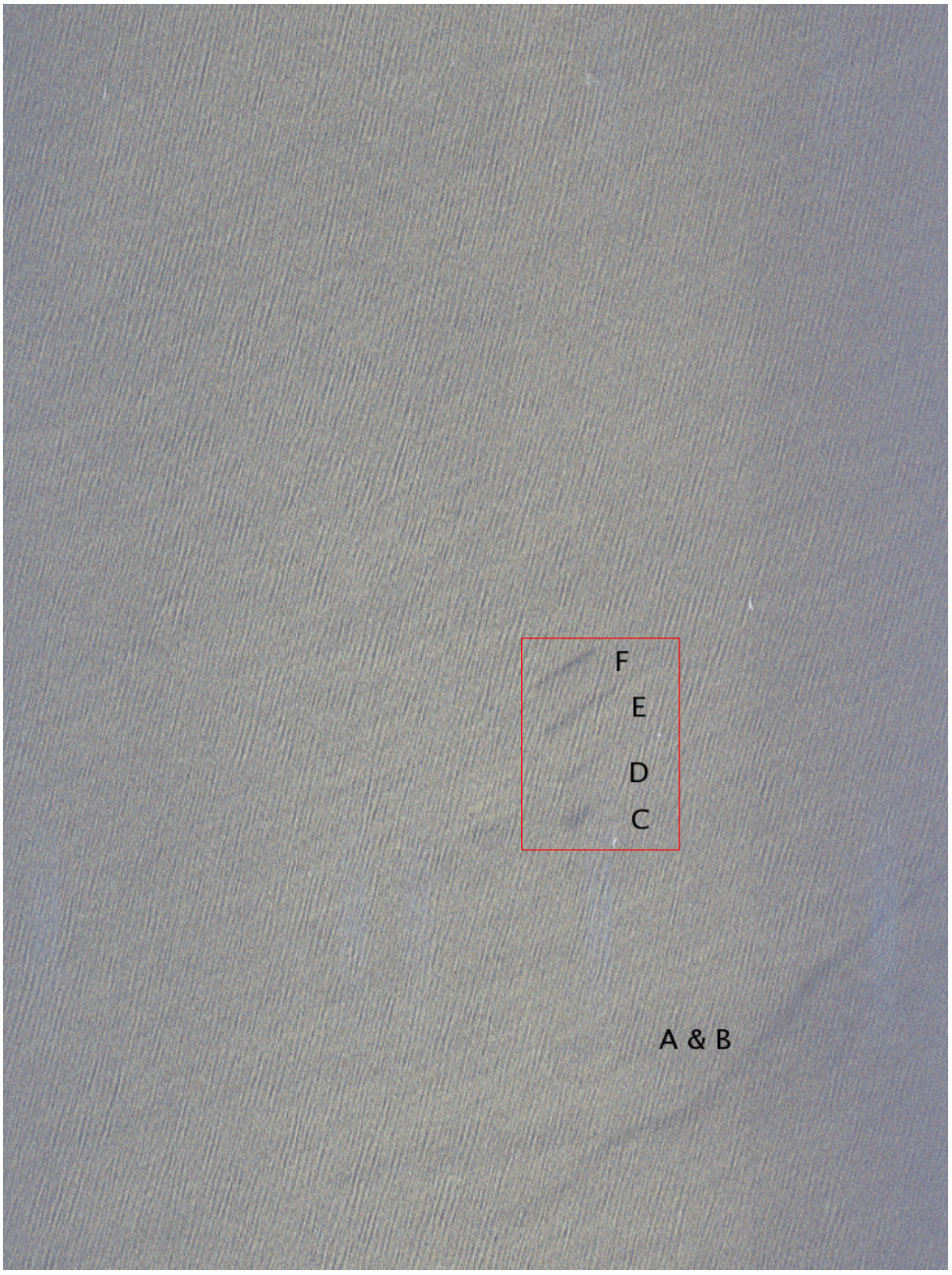

Figure 5.3: Scene 2, full scene. The red square is the subscene that is considered in this thesis, and which is showed in further detail in figure 5.4. The letters A-F are detailed in table 5.3. Slick A and B appear to have merged, likely due to the weather conditions and the time passed since the discharge. RISAT-1 ©2015-Antrix, processed by KSAT, all rights reserved 2015.

Table 5.4: Scene 2, metadata

Satellite	RISAT-1
Processing station	KSAT
Imaging date	10 June 2015
Product ID	1530741004
Scene start time	07:19:18.536 UTC
Scene center time	07:19:20.836 UTC
Scene end time	07:19:23.136 UTC
Imaging orbit number	17197
Processing Level	SLC
Imaging mode	FRS-1
Polarization	RH + RV
Sensor orientation	Right
Orbit node	Descending
Incidence angle	44.02802°
Satellite altitude	547.710 km
Line spacing	2.41
Pixel spacing	1.80
Noise equivalent sigma zero (NESZ)	−16.7999992
Calibration Constant γ_0, RV	69.439
Calibration Constant γ_0, RH	72.581
Calibration Constant β_0, RV	69.294
Calibration Constant β_0, RH	72.437

from the oil industry, recognition and detection companies, the Norwegian Coastguard, the Coastal administration, pollution authorities and research institutions. Oil is discharged from ships in controlled, specified amounts at various locations. Vessels, aircraft and satellites, then use numerous different sensors such as SAR, to detect and/or characterize the slicks. The main objective of the exercise is to test procedures and equipment for oil spill response. The fact that everything is controlled, and that there are personnel on site when the discharge is being done and all through the exercise, makes for valuable in situ data.

As the scene was recorded during the 2015 OoW exercise, the features in the scene as well as the in situ data, are described with an accuracy and a confidence rarely found in other data sets.

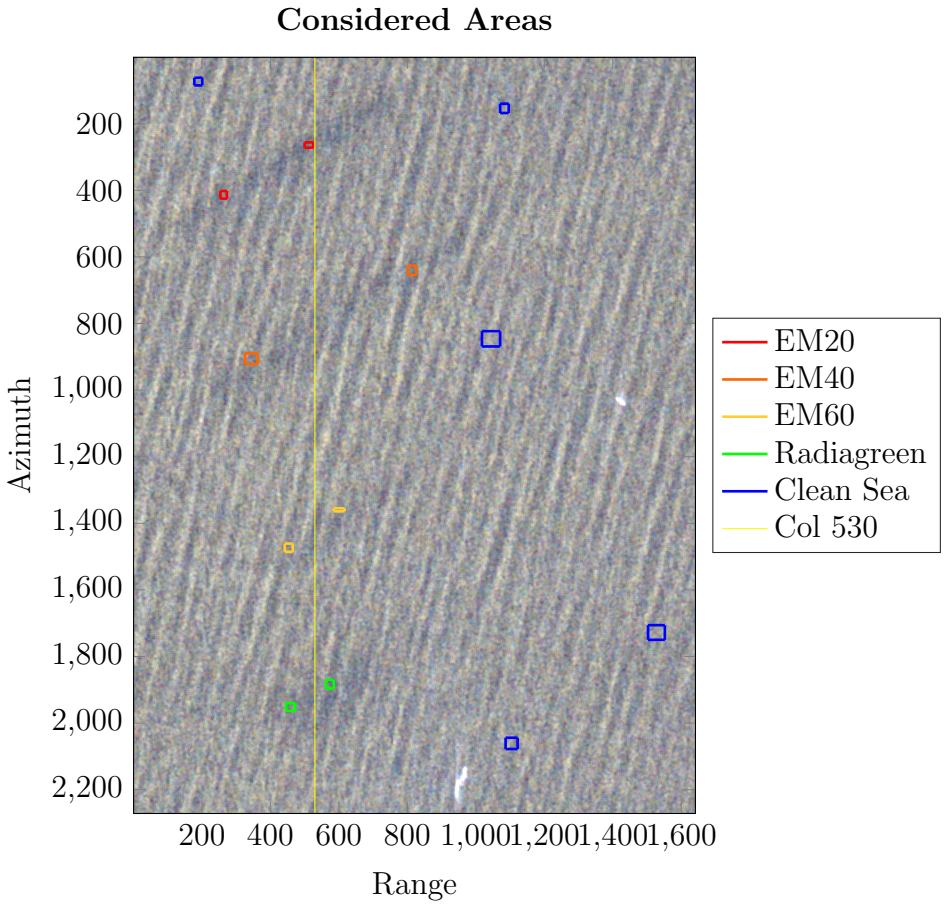

Figure 5.4: Sub-scene of Scene 2. Areas used for calculations are marked by coloured rectangles, where red is EM20, dark orange is EM40, light orange is EM60, green is Radiagreen, and blue is Clean sea. The yellow vertical line is used to compare values across the image and through all the slicks. RISAT-1 ©2015-Antrix, processed by KSAT, all rights reserved 2015.

Chapter 6

Results & Discussion

In this chapter, the results from the analysis of the HP features extracted from scene 1 and scene 2, will be presented and discussed. In addition, a noise analysis made on the unfiltered SAR data will be performed and presented. Eventually, the HP features will be compared against each other to see which is the better option for oil spill detection.

For reading the RISAT-1 images, ESA PolSARpro version 5.0.4 was used. This program reads the encrypted product files and converts them to a decrypted bin file format. The two resulting files s11.bin and s21.bin (the Sinclair elements), contains the real and imaginary values of the SAR scene in an alternating column pattern per scene row, such that for every pixel in the scene, there are one row value and two column values in the bin file. A MATLAB function was created to read the bin files and convert them to one complex double matrix per polarization (RH and RV).

6.1 Noise Analysis

In this section, the noise analysis of the evaluated scenes will be described. The analysis tells something about how well the signal can be separated from the noise, and how much of the signal is likely to be corrupted by the background noise.

It is noted during the literature study for this thesis, that most of the articles on HP parameters have omitted to perform a noise analysis.

The NESZ, also known as the noise floor, is the background noise in the SAR

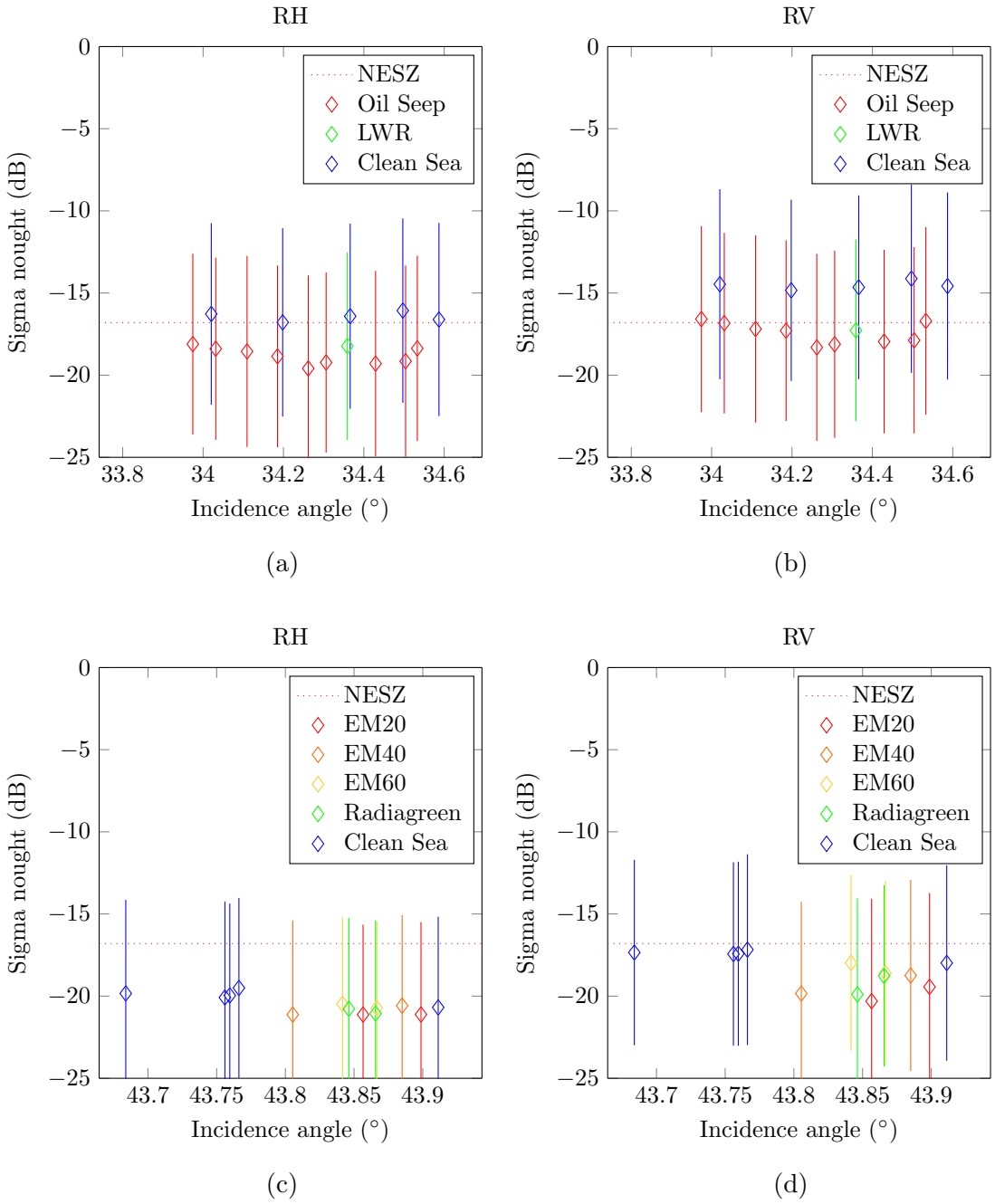

Figure 6.1: Signal-to-noise analysis for the two RISAT-1 scenes described in table 5.1, where (a) and (b) are values for Scene 1, RH and RV channel respectively, and (c) and (d) are values from Scene 2, RH and RV channel respectively. The diamonds represent the mean value of the regions specified in the figures 5.2 (corresponding to (a) and (b)) and 5.4 (corresponding to (c) and (d)), while the vertical bars equals one standard deviation above and below the mean.

system. It is a measure of the radar sensitivity to low-backscatter areas. If the measured Normalized Radar Cross Section (NRCS) is equal to or below the NESZ for any features, these will be corrupted by the instrument noise, and thus largely unsuitable for analysis of backscatter properties. However, oil slick *detection* may still be possible, as long as the backscattered intensity from the oil and the surrounding clean sea is different. The problem occur when we try to characterize the feature in the SAR image. We may be able to detect a feature that is separable from the surrounding area (sea) as a black feature. However, if the signal is corrupted by noise, it is not possible/very difficult to characterize different types of slicks, at least without additional information.

For most SAR instruments, NESZ will vary across the beam swath, and in general be lower towards the center of the beam (in range). RISAT-1 however, has been designed to maintain a near constant NESZ across track[14]. For RISAT-1 products (in CEOS format) the NESZ is given in the product's lea_01.001.dat file.

Compared to RADARSAT-2, the NESZ for RISAT-1 is relatively high. RADARSAT-2 Standard QP SLC products have an estimated NESZ of -38 ± 3 dB[27], while RISAT-1 FRS-1 products have an estimated NESZ of about -16.8 dB.

Signal-to-noise analysis has been performed on the sigma nought for the evaluated scenes. This is done *prior* to any modifications to, or manipulation of the data, and there has *not* been done any smoothing/speckle filtering in order to maintain the original quality of the data. Figure 5.2 and figure 5.4 show the areas considered for calculating mean and standard deviations for oil covered and clean sea water. The result is displayed in figure 6.1. The mean is represented by diamond shapes, and the vertical lines represent the standard deviation.

For both scenes, the response in the RH channel is lower than in the RV channel. This is to be expected, as it is known that VV polarization is more sensitive to Bragg scattering than HH polarization, i.e. $|S_{HH}|^2 - |S_{VV}|^2 \leq 0$[52], and assuming the same property is valid for RV and RH polarizations.

For the Cantarel scene, the mean for clean sea is above the NESZ in the RV channel. However, both wind shadows and oil seep is mainly below the noise floor. Minchew et al.[28] state a power threshold of 6dB to be the minimum distance from the NESZ in order to distinguish the signal without significant corruption by the instrument noise, using UAVSAR L-band SAR data covering the DWH oil spill. If considering this a likely and reliable measure also for the RISAT-1 FRS-1 data considered in this thesis, it is seen that even the RV channel in the Cantarel scene, although above the NESZ, is in the area considered likely to be corrupted by noise.

The OoW scene shows an even lower signal response, with all values very close to, or below the noise floor, even in the RV channel. This means that the signal is even more likely contaminated by noise, which will make analysis and categorization for this scene even more difficult.

It has been proven that backscatter from the ocean surface will decrease with increasing incidence angle[11]. The incidence angle is quite a lot higher for the OoW scene than it is for the Cantarel scene, which may partly explain why the signal is weaker for the OoW scene.

6.2 The Normalized Distance between Samples

To measure the statistical distance between the different samples of clean sea, oil covered water and LWR, the d_{norm} was calculated for all parameters including the individual Stokes parameters and the original sigma nought images for each channel. The d_{norm} is defined as

$$d_{\text{norm}} = \frac{|\mu_1 - \mu_2|}{\sigma_1 + \sigma_2} \tag{6.1}$$

where μ represents the mean and σ represents the standard deviation, and the subscripts 1 and 2 indicate the two different sample areas.

The d_{norm} was also used by Li et al.[23] to calculate the statistical distance between QP and HP SAR features. Others, such as Salberg et al.[40] has chosen to use the Bhattacharyya distance, but according to Li et al.[23], these measures (including the Modified Distance between Samples, J_d) have a very similar performance when measuring the statistical difference between polarimetric SAR features. In this thesis, the d_{norm} will be used.

The results from the calculation of d_{norm} are listed in table 6.1, and will be further discussed in the following sections.

Table 6.1: The normalized distance between samples for the LWR and the oil in scene 1, and the different oil types and look-alike in scene 2, compared to the samples of clean sea (see figure 5.2 and figure 5.4, respectively). The parameter with the highest contrast is marked in bold for all features.

	Scene 1		**Scene 2**			
	Oil seep Clean sea	**LWR Clean sea**	**EM20 Clean sea**	**EM40 Clean sea**	**EM60 Clean sea**	**Radiagreen Clean sea**
RH	0.1940	0.1232	0.0991	0.0747	0.0541	0.0803
RV	0.2251	0.1414	0.2053	0.1597	0.0728	0.1631
S_1	**2.2401**	1.5527	**1.6233**	**1.1316**	**0.7671**	**1.1748**
S_2	1.0556	0.8278	1.3618	1.0268	0.4241	1.0094
S_3	1.5383	1.2971	0.5130	0.6245	0.7089	0.4784
S_4	2.1101	1.9280	1.3317	0.9386	0.6515	1.0199
χ	0.1565	0.4768	0.2946	0.0783	0.1570	0.2398
DoP	1.5699	1.8836	1.3132	1.0469	0.5303	0.9507
$m - \chi$	0.9021	0.6586	0.8023	0.8543	0.3258	0.7781
H	1.6687	**1.9282**	1.3231	0.9194	0.5215	0.9552

6.3 Stokes Parameters

When calculating the Stokes parameters, a sliding window averaging filter of 15x15 pixels has been used, which reduces the speckle noise.

The Stokes parameters actually form the basis for all of the parameters considered in this thesis. However, it is also useful to consider the parameters themselves, as they are.

In figure 6.2 and 6.3, the Stokes parameters are presented individually for scene 1 and scene 2, respectively. In figure 6.2 the leftmost column show the Stokes parameters as individual intensity images with S_1 on the top and S_4 on the bottom. The middle and right columns represent the values along the pink and yellow transact lines in figure 5.2, respectively, and are ordered like the first column. In figure 6.3, the left column shows the intensity image of the Stokes parameters, while the right column show the intensity values along the yellow transact line as outlined in figure 5.4. The dark patches and spots are NaN-values where man-made objects and speckle noise have been masked out.

From a visual inspection of figure 6.2, it is seen that it is relatively easy to distinguish the oil from the clean sea for all parameters. The strongest contrast is for S_1 (figure 6.2a). S_1 also has got higher values over-all than the other three parameters. This is perhaps natural, as S_1 is defined as the total power (density)

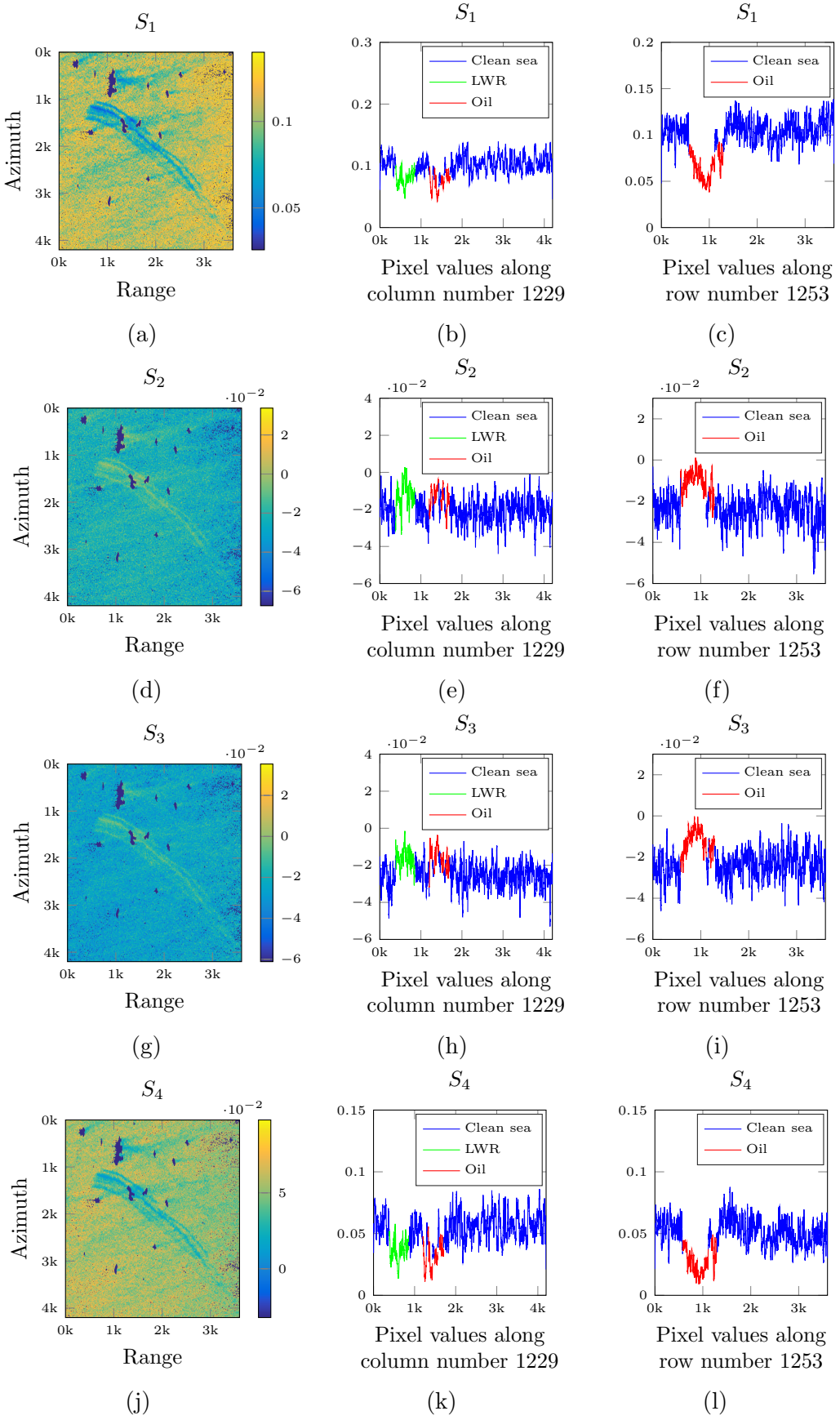

Figure 6.2: The leftmost column show the four Stokes vectors as calculated for scene 1, starting with S_1 on the top, down to S_4 on the bottom. Values for the corresponding Stokes vectors for scene 1, along the pink and yellow transact lines shown in figure 5.2 are shown in the middle and rightmost column, respectively.

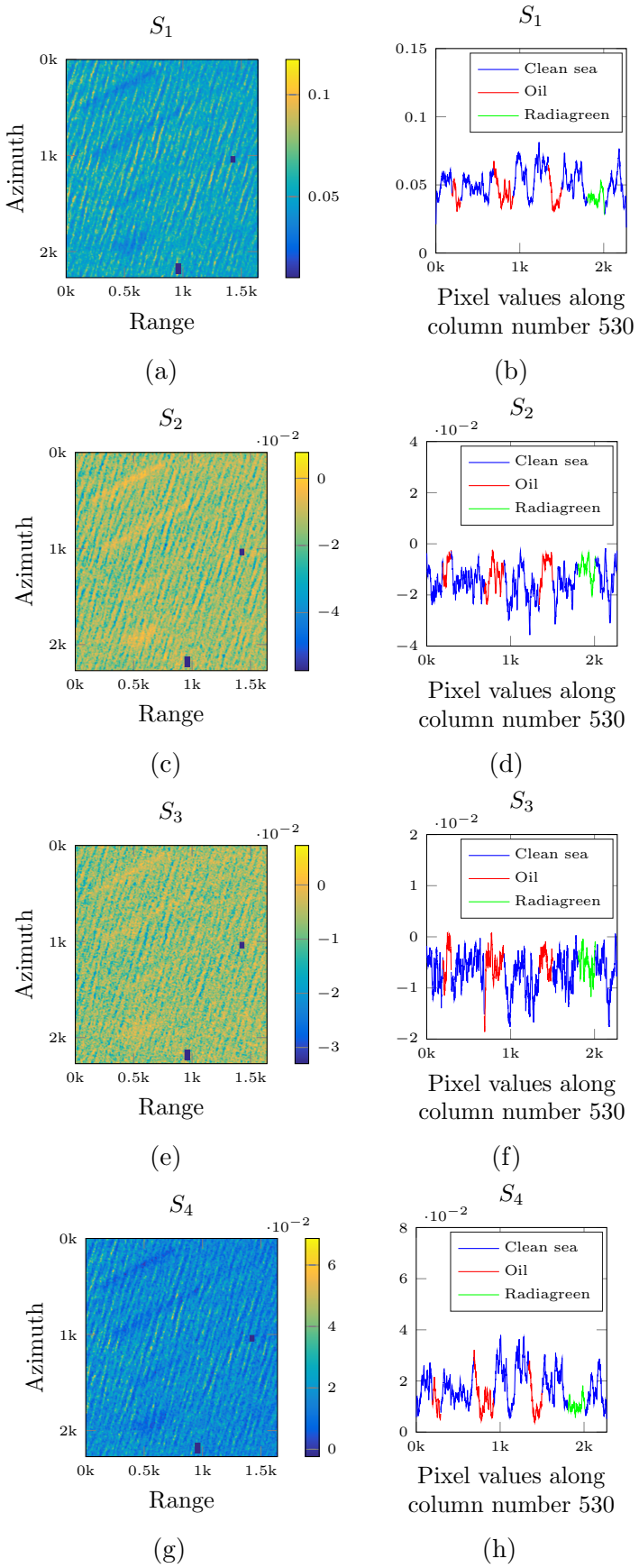

Figure 6.3: The left column show the four Stokes vectors as calculated for scene 2, starting with S_1 on the top, down to S_4 on the bottom. Values for the Stokes vectors along the yellow transact lines shown in figure 5.4, are shown in the right column.

of the backscattered wave, and thus equals the sum of the other three parameters squared (3.5). It is observed that for both S_2, S_3 and S_4, the slicks have values closer to 0 than clean sea. I.e., S_2 and S_3 both have negative values and the slick has got higher value than the clean sea, but this does not change the fact that the slick has intensity value closer to 0 than the clean sea. So, when squaring, the sign is reversed, and now the sea has got the highest value, and the slicks have a lower value. This correspond with the original values for S_4, which of course have no sign change as positive squared is still positive. Hence, we have three low values for oil which is summed, and three high values for clean sea which is summed. The result is that the dynamic range is stretched, and we also get an overall rise (although perhaps very slight) in the values. A stretched dynamic range should make the slicks more visible when displayed as an intensity image.

S_4 (figure 6.2j) is second-best, with quite good contrast between the oil and the clean sea. It also appear to even out the surroundings more than S_1, but it is difficult to distinguish between oil and the LWR. Compared to S_2 and S_3, S_4 have larger intensity values over-all. The S_4 is equal to the power of the left-handed and right-handed circularly polarized field.

S_2 (figure 6.2d) and S_3 (figure 6.2g) has almost the same performance, but S_3 appear to be slightly better than S_2 at distinguishing the oil. S_2 and S_3 also have the lowest values overall. Almost all the values are below zero, apart from a few pixels within the oil-covered and LWR areas. Additionally, S_2 and S_3 appear to be slightly more influenced by noise in far range than S_1 and S_4, although all parameters are noticeably affected by noise when approaching far range.

S_1 and S_4 show lower values over the oil slicks compared to clean sea, while the opposite is true for S_2 and S_3. It is also seen that for S_1, the value of the clean sea increases very slightly towards the far range, while for S_4, the value for clean sea decreases towards far range. Both S_2 and S_3 has more evenly distributed pixel values for clean sea along the incidence range.

The values for S_2 and S_3 are all below zero, but over oil, the values approach zero. I.e., over oil, the linear horizontal and vertical polarized components approach each other and become more equal (see equation (3.2)). Over sea, the horizontal response has a lower intensity than the vertical response, as is seen by $J_{RH} - J_{RV}$ giving a negative value. So, oil on the sea surface appear to increase the horizontal response or decrease the vertical response, or both.

Also when visually inspecting figure 6.3, it is seen that it is relatively easy to distinguish oil from the clean sea in all images. However, there is a very pronounced, slightly diagonal wave pattern that is disturbing the interpretation significantly.

The wave pattern is also visible within the slick areas, further adding to the complexity of the analysis for this particular scene.

Apart from the wave pattern, much of the same effects are seen in scene 2, as was seen in scene 1. The S_1 is still the parameter with the highest values over-all. S_4 has got lower values over-all than S_1, but larger than S_2 and S_3. For S_1 and S_4, the values over oil-covered water is lower than the clean sea, while for S_2 and S_3 it is the opposite.

The values for S_2 and S_3 are mostly below zero, apart from a few pixels within the oil slick for S_3. However, while it was S_3 that had the lowest over-all values for scene 1, it appears that for scene 2, S_2 is the parameter with the lowest over-all values.

In the stripe values in the right-most column of figure 6.2, it does however become very obvious how significant the impact of the wave pattern is. The intensity value range for clean sea completely overlaps with the intensity value range for oil and Radiagreen. It is thus simply impossible to threshold any values with the purpose to detect oil using these parameters, for this particular scene. Pattern recognition or similar techniques may help, but even with pattern recognition as part of an automatic analysis, the oil could ”hide” within the wave pattern and would then be next to impossible to detect, even for a trained operator.

In addition, it is impossible to separate the look-alike (Radiagreen) from both oil and/or clean sea. It may have been different without the presence of the wave pattern, but to establish a trustworthy result for the purpose of distinguishing look-alikes from oil, and oil from sea water, more research is needed.

From the d_{norm} values listed in table 6.1, it is seen that for scene 1, S_1 and S_4 have the best performance by far compared to the other HP parameters considered in this thesis. This is not as pronounced for scene 2, where there also are other parameters with similar performance, however S_1 and S_4 are still amongst the best. The d_{norm} values confirm the visual impression for scene 1, that S_1 is slightly better than S_4, which is quite much better than S_3 which again is better than S_2 for distinguishing oil from the clean sea. It does however seem like S_1 is better at dampening the response (i.e., it has a lower d_{norm} value) from the LWR than S_4, which is slightly surprising.

There are no LWR to be considered in scene 2, and the d_{norm} value for S_1 is higher than for all the other parameters when calculated for Radiagreen versus clean sea. However, S_1 also outperforms all the other evaluated parameters for distinguishing emulsion (regardless of concentration) from clean sea. As mentioned, not by as

large a margin as for scene 1, but it is still the best option. What is interesting, is that for scene 2, S_2 is the next in line for Oil Emulsion containing 20 % water (EM20), although it is not as good as S_3 for distinguishing Oil Emulsion containing 40 % water (EM40) and Oil Emulsion containing 60 % water (EM60) from clean sea. The reason for this could be one or more of many, e.g. the concentration of the oil, the thickness of the oil, (very) local wind and wave patterns, ships disturbing the spill, etc. More research is needed to establish a circumstance where the sensitivity shifts from S_2 to S_3 and vice versa.

Li et al.[21] found that S_2 was suitable for automatic oil spill detection algorithms based on the Otsu threshold (see chapter 4.1). There was no noise analysis performed by Li et al.[21], but Skrunes et al.[44] did perform a noise analysis on the third of the three scenes, from 8 June 2011. The noise analysis showed that for the co-polarized channels, most of the values were within one standard deviation of the noise floor, with the mean HH values being about $0.7 - 1.5$ dB below the mean VV values in the slick-covered areas. The mean values were $10.1 - 12.3$, $5.9 - 7.2$, $3.8 - 5.6$ and $14.1 - 15.8$ dB above the NESZ for plant oil, emulsion, crude oil and clean sea, respectively.

For the cross-pol channels however, the results were much worse, with all values within one standard deviation below the NESZ. According to Minchew et al.[28], all values less than 6 dB above the NESZ are considered to be corrupted by instrument noise, and thus not suitable for analysis of the scattering properties. From the noise analysis it is seen that even for the co-polarized channels, the response from the crude oil, and also partly the emulsion, should be considered contaminated by noise if the definition from Minchew et al.[28] is to be followed.

By just focusing on S_2, Li et al.[21] will have to rely on the backscattered power from the linear horizontally and vertically polarized components not being significantly corrupted by noise. That may be the case for this scene, but it may also be the reason why this scene is the most difficult to perform the Otsu threshold method on, given the result from the noise analysis by Skrunes et al.[44].

The results in this thesis does not support the choice of S_2 as the better parameter for distinguishing oil from clean sea, but it should be mentioned that the scenes used for this thesis is heavily affected by noise. The incidence angle between the third scene considered by Li et al.[21] and scene 1 is very similar, but the NESZ is much higher for RISAT-1 than for RADARSAT-2. This, and the fact that this thesis is based on actual HP data compared to the simulated data used by Li et al.[21], may have had an impact on the results.

6.4 The Degree of Polarization

Figure 6.4 show the results of the DoP applied to scene 1 and scene 2, respectively. Figure figs. 6.4a to 6.4c represent the intensity image of the DoP for scene 1, and the intensity values along the pink and yellow transact lines outlined in figure 5.2, respectively. Figure figs. 6.4d and 6.4e represent the intensity image of the DoP applied to scene 2, and the intensity values along the yellow transact line outlined in figure 5.4, respectively. The dark patches and spots seen in the intensity images are NaN values where man-made objectes and speckle noise have been masked out.

From figure 6.4a it is observed that the values for oil-covered water approaches zero, while the clean sea levels are somewhere just above half-way up the colourbar. So, the backscattered wave is more depolarized over the oil-covered water than it is for clean sea. However, the values over clean sea decline in the far range region, and get more close to the values for oil-covered water, i.e. all received backscatter get more depolarized. It is also noticed that the speckle noise is much more pronounced for this region.

The visual impression is supported by the values in figures 6.4c. It is clearly possible to separate the oil from the clean sea, but it gets harder towards far range, as we can see that the intensity values for clean sea approach the same region as the oil-covered water. Along column 1229, as visualized in figure 6.4b, it is clearly possible to separate oil and the LWR from the clean sea, but it is not easy to separate the LWR from the oil.

In figure 6.4d it is obvious that the slightly diagonal wave pattern is still heavily affecting the results. It is hard to see the difference between the darkest parts of the wave pattern, and the oil slicks and the lookalike. Still, due to the shape and orientation of the slicks, they are clearly visible to the eye. It would however not be easy to distinguish automatically using this parameter, as the disturbance from the waves are this pronounced.

The intensity values shown in figure 6.4e support this interpretation, as the values are more or less in the same region regardless of what is illuminated by the sensor.

Still, the same characteristics as found for scene 1 is seen also for scene 2. The oil-covered areas approach zero (more depolarized), and the clean sea in general is just above the middle of the colourbar. It is just that the wave patterns in clean sea areas get a similar signature as oil-covered water, i.e. some parts of the wave pattern are more depolarized and resembles the oil (and the look-alike).

Considering the d_{norm} values presented in table 6.1, it is seen that DoP is not as

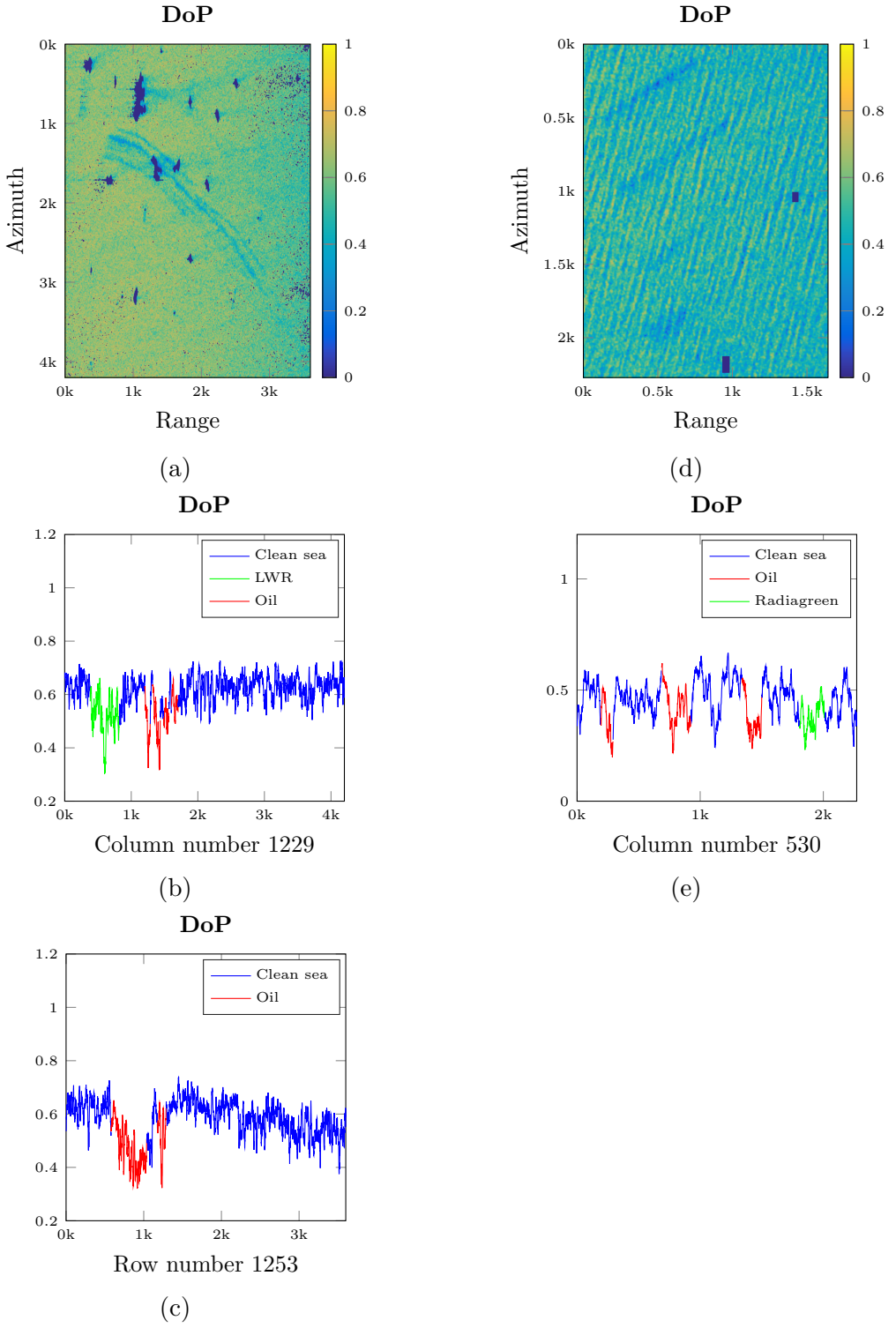

Figure 6.4: (a) show the DoP for Scene 1. (b) and (c) show the values for DoP along the yellow and pink lines shown in figure 5.2, respectively. (d) and (e) show the DoP for Scene 2 and the values for DoP along the yellow line shown in figure 5.4, respectively. The dark patches are NaN values where man-made objects has been masked out, and the smaller dark spots are speckle (salt) noise which have also been masked out.

good for distinguishing between oil and clean sea, as the stokes parameters S_1 and S_4.

Shirvany et al.[43] found that the DoP was useful for detecting and characterizing both oil and man-made structures at sea. Li et al.[20] found that the DoP was more sensitive to different types of oil spill than the χ. It was also found that the DoP decreases when the incidence angle increases, which corresponds well with what is found in this thesis. However they also found that the separation between clean sea and oil increased by higher incidence angle, which is not what is observed in this thesis.

The results in this thesis supports that the DoP is able to separate oil from clean sea, and should also be better at separating different oil concentrations even with a low SNR. It is however also sensitive to the variable backscatter in range, if the backscatter is close to or below the NESZ.

6.5 The Ellipticity Parameter

The result of the ellipticity parameter (χ) for scene 1 and scene 2 are shown in figure 6.5a and 6.5d, respectively. A sliding window averaging filter of size 15×15 was used to calculate the Stokes Parameters which form the basis of the χ (see equation 4.8, chapter 4.3).

From visual inspection, it is observed that the contrast between the oil spills and the clean sea, and also the contrast between the wind shadows and the clean sea, nearly disappears. Compared to the unmodified figure 5.2 and 5.4, it is clearly more difficult to distinguish the oil from the background. There could be several reasons for this, including the incidence angle, the SNR, the weather conditions, etc. In any case, the conclusion is that for *visual* oil spill detection, the χ does not add anything to the scenes considered in this thesis. In fact, applying the χ makes visual analysis more difficult, compared to the single channel intensity images.

The values along the yellow line in figure 5.4, are given in figure 6.5d. The red colour is approximately indicating oil-covered water, while the blue colour represents clean sea. From the graph it is not really possible to distinguish between the different concentrations of oil and the clean sea in scene 2, which confirms the visual interpretation.

To draw a single line to capture part of the oil spills with the strongest contrast to the sea as well as the LWR in scene 1 was difficult, so two lines were drawn,

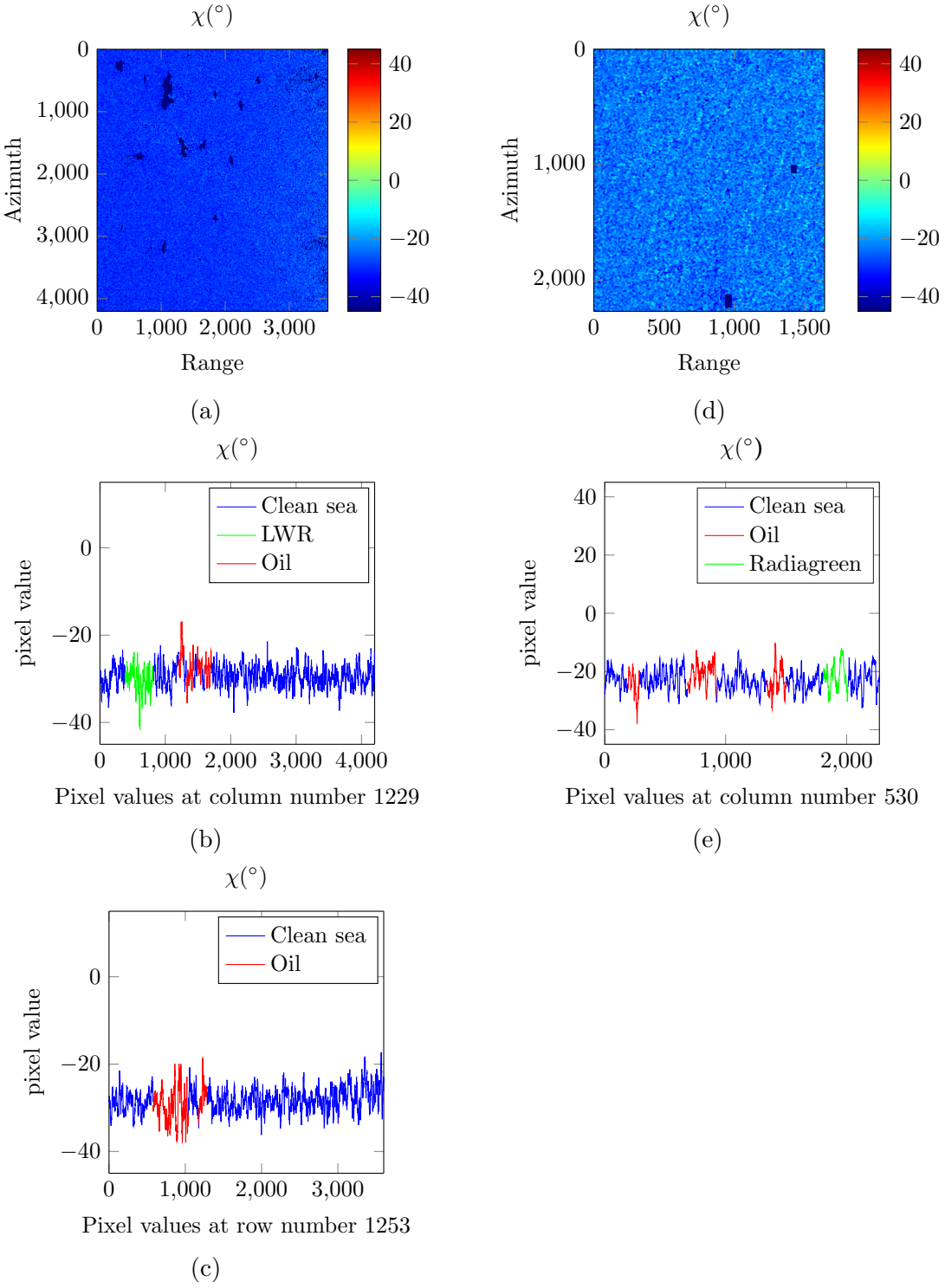

Figure 6.5: (a)-(c) show the χ calculated for scene 1, the values for χ along pink and yellow line in figure 5.2, respectively. (d) and (e) show the χ calculated for scene 2, and the values for χ along the yellow line shown in figure 5.4, respectively. The dark patches are NaN values where man-made objects have been masked out.

seen as a horizontal yellow line and a vertical pink line in figure 5.2. Figure 6.5c and 6.5b show the results for the yellow and the pink line, respectively. In 6.5b, the green colour represents the LWR, while the blue and red are clean sea and oil, respectively. In 6.5c, the red colour represents oil-covered water, while blue is clean sea.

A slight difference between the three oil slicks and the look-alike may be seen in the values in figure 6.5b, but not enough to positively differ between them. And although there are peaks within the oil and the LWR, the signal still varies too much within and across the regions to positively distinguish between LWR, oil and clean sea based on this graph.

According to the values for d_{norm} given in table 6.1, the χ gives the smallest statistical distance between oil seep and clean sea of all the measured parameters, but not the smallest statistical distance between LWR and clean sea, in scene 1. Also for scene 2, the performance according to the d_{norm} values are among the worst of the considered parameters.

The sign reversal that was found by Li et al.[20], was found in a RADARSAT-2 scene where the incidence angles spanned from 41.9° to 43.4°. The scene that did not show a sign reversal, had incidence angles from 29.2° to 30.9°. In the datasets considered in this thesis, Scene 1 has incidence angles from 34.22° to 34.69°. Scene 2 has incidence angles from 43.66° to 43.94°.

Salberg et al.[40] also suggests that there may be a relation between the incidence angle and the response from χ. In their article, the colour of the oil slick changes in some scenes from dark to bright, which could be due to a sign reversal or similar effect. The effect seem to occur at about 35°, where any slicks below this limit has a bright response and slicks above this limit have a dark response compared to the surrounding clean sea. The scenes considered in this thesis appear to have a slightly stronger contrast between oil and clean sea at 44° than at 34°, which corresponds somewhat to what is observed by Salberg et al.[40].

Comparing incidence angles alone, scene 2 is closest to the scene where Li et al.[20] observed the sign reversal effect, and scene 1 is closer to the incident range of the DWH scene considered by Li et al.[20]. The different incidence ranges is visualized in figure 6.6. In the scenes considered in this thesis, no sign reversal was observed. This suggests that either the scene considered by Li et al.[20] was just far enough from scene 2 to reach some ”sweet spot” in the incidence angle range where sign reversal can/will occur, or that there are other factors that are also important for getting this effect in the signal backscatter.

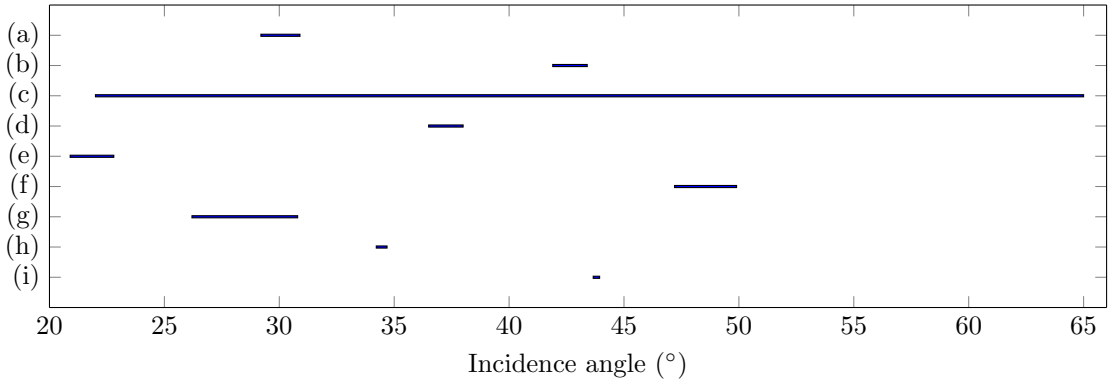

Figure 6.6: Incidence angle range for (a) RADARSAT-2 DWH scene considered by Li et al.[20], (b) RADARSAT-2 Seep scene considered by Li et al.[20], (c) the two UAVSAR scenes considered by Li et al.[20], (d) The RADARSAT-2 scene covering Penglai 19-3 oilfield considered by Yin et al.[52], (e) the RADARSAT-2 scene covering Dalian port considered by Yin et al.[52], (f) the SIR-C scene numbered 49939 considered by Yin et al.[52], (g) the SIR-C scene numbered 41370 considered by Yin et al.[52], (h) Scene 1 and (i) Scene 2.

According to the threshold suggested by Minchew et al.[28], the scenes considered in this thesis are corrupted by instrument noise (section 6.1). Consequently, it is necessary to assume that the noise may cause problems for oil spill classification in the considered scenes. Looking at the results from Li et al.[20] however, it appears that in the scene where the sign reversal was observed, the signal return from the oil slicks are very close to the NESZ, while the surrounding area is about 10 dB above the NESZ. In the second scene, where the sign reversal did *not* occur, the backscatter values from the oil slicks looks to be about $5-7$ dB above the NESZ, with the surrounding area is about 12 dB above the NESZ. We therefore suggest that the sign reversal may occur when the signal response get close to the NESZ, rather than because of the incidence angle alone (of course, the signal response will also vary with the incidence angle). The conclusion in this thesis is therefore that the sign reversal is not a definite descriptor for oil slicks. In fact, it is likely that the sign reversal may appear also for other dark patches when the signal response over the patch comes close to the NESZ.

Unfortunately, the NESZ and SNR are not given in the article by Salberg et al.[40], nor are there any colourbars to allow making assumptions for these values, such as was possible in the article by Li et al.[20], and no noise analysis has been performed for the evaluated scenes. For these reasons, it is difficult to tell where the backscattered return is compared to the NESZ, and thus if or to what extent the noise have had any impact on their results. However, Skrunes et al.[44] did perform a noise analysis for the first scene that was used by Salberg et al.[40], so for this scene it is possible to find information about the SNR. This was the scene with

incidence angle at 35 deg, and it is also one of the scenes where the χ gave a bright response. From the noise analysis performed by Skrunes et al. [44], it is clear that this particular scene had a bad SNR, with most of the signal values within one standard deviation below the noise floor.

From the results found in this thesis, there are no clear indications that the χ should be directly affected by the incidence angle, as suggested by Li et al. [20]. However, the incidence angle will affect the backscattered signal, which again means that for some incidence angles, the signal is closer to the NESZ than for other incidence angles. In this respect, it is plausible that the incidence angle is one of the contributing factors for the sign reversal observed by Li et al. [20]. However, it is not just the incidence angle that determines how close the backscattered signal get to the NESZ. Wind/weather conditions, ocean currents, oil properties and the SNR are also important factors deciding the backscattered signal. Therefore, it is not sufficient to state that sign reversal of the χ depends on the incidence angle alone. It is however plausible that the sign reversal appear when the backscatter is close to the NESZ, and it is likely that all areas close to the noise floor could give such a response, be it oil or other features (e.g. LWR). Unfortunately, the SNR of the scenes considered in this thesis are probably too low to confirm or reject this statement, as the backscatter is below or very close to the NESZ.

6.6 The $m - \chi$ Decomposition

Figure 6.7 shows the $m - \chi$ decomposition applied to scene 1, while the result for scene 2 is shown in figure 6.8. In both these figures, (a) show the $m - \chi$ visualized as an RGB image, as suggested by Raney et al. [36] (section 4.4, equation 4.9), while (b), (c) and (d) show the individual red, green and blue channels, respectively. When using this visualisation method, red represents the double-bounce response, green indicate the randomly polarized constituent, and the blue channel correspond to the single-bounce (and Bragg) backscatter. [36]

As figure 6.7a and 6.8a clearly show, visual analysis of the considered scenes after the $m - \chi$ decomposition has been performed, is next to impossible, at least for the considered scenes. It is however possible to distinguish oil from clean sea in the red and the blue channel, and the slicks are vaguely visible also in the green channel. It should be noted that the colour scale has been modified to span only the actual values in (b), (c) and (d) to further enhance the dynamic range.

From the figures, it appears that the contrast between the oil and the clean sea is

best when single- and double-bounce is favoured, compared to randomly polarized backscatter.

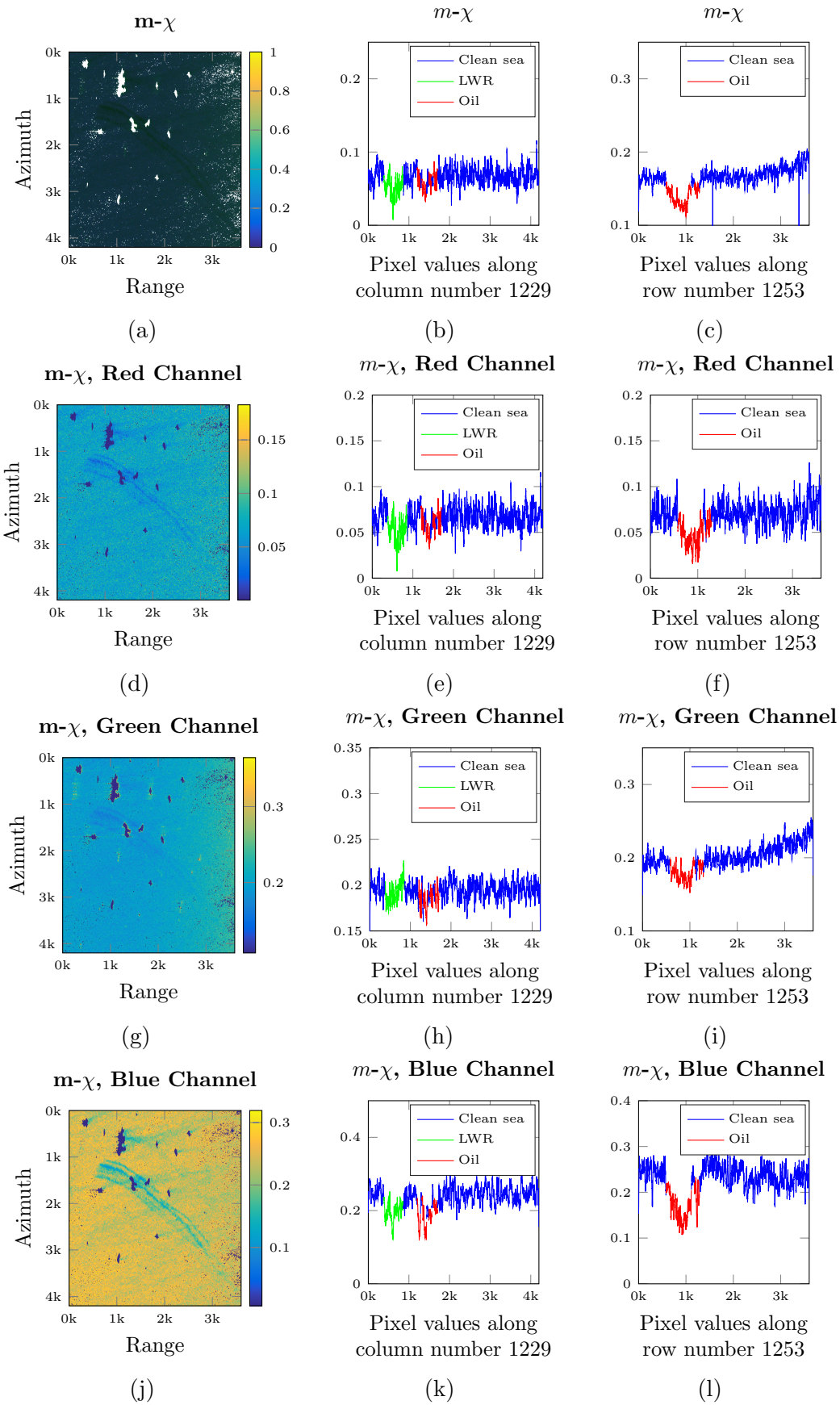

Figure 6.7: The left column show from top to bottom the $m-\chi$ decomposition as an RGB-coded image, then the red, green and blue channels, respectively. The white patches and spots in the RGB image, and the dark patches and spots in the individual channel images are NaN values where Man-Made objects and speckle noise have been masked out. The middle and rightmost column show values from the corresponding image in the left column, as along the pink and yellow transact lines shown in figure 5.2, respectively.

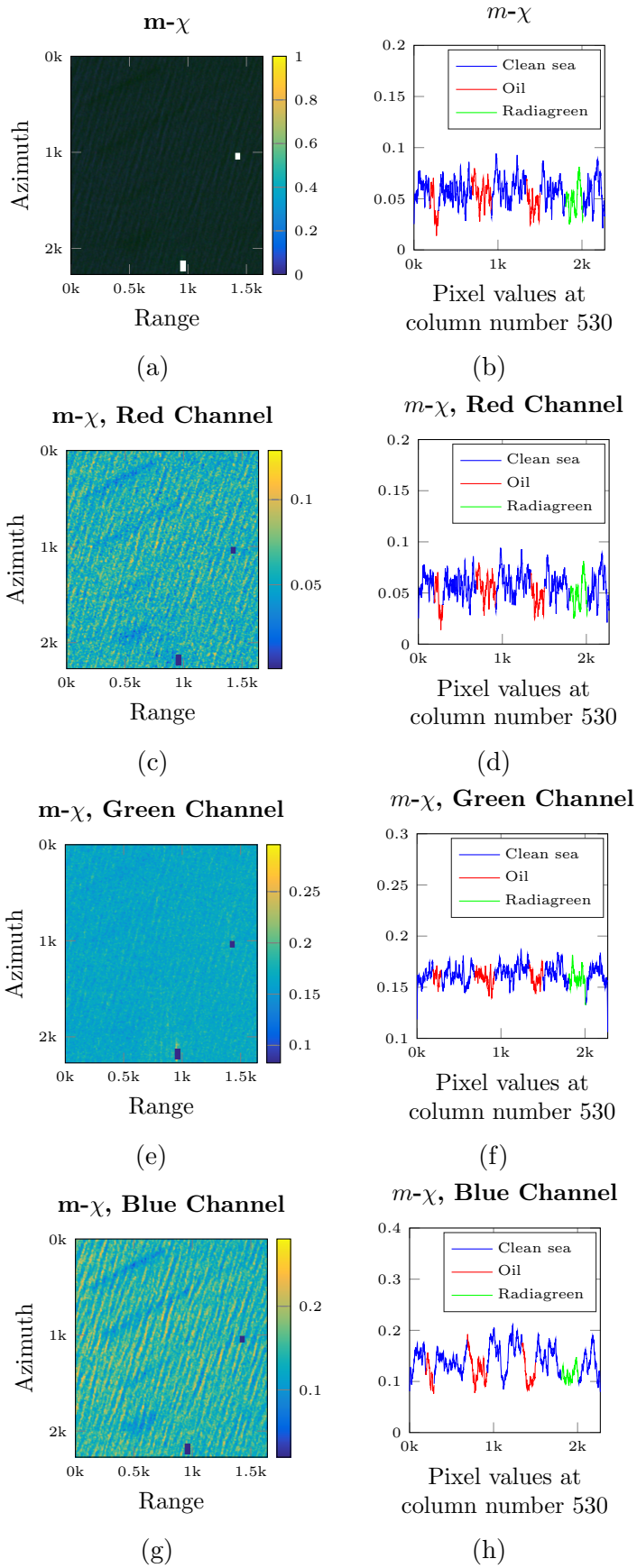

Figure 6.8: The left column show from top to bottom the $m-\chi$ decomposition as an RGB-coded image, then the red, green and blue channels, respectively. The dark patches and spots are NaN values where Man-Made objects and speckle noise have been masked out. The right column show values from the corresponding image in the left column, as along the yellow transact lines shown in figure 5.4.

6.7 The Entropy

Figure 6.9 show the result from the calculation of entropy for scene 1 and scene 2, respectively. Figures figs. 6.9a to 6.9c show the intensity image for the H, and the intensity values along the pink and the yellow transact lines outlined in figure 5.2, respectively. Figure figs. 6.9d and 6.9e show the intensity image of the entropy applied to scene 2 and the intensity values along the yellow transact line outlined in figure 5.4, respectively.

Looking at figure 6.9a, it is observed that oil-covered water is approaching the maximum value of 1, and that it has a higher value than clean sea, which is closer to ~0.7. As the incidence angle goes towards far range, the general value level increases, and all values approach 1. This is confirmed by figure 6.9c, where it is obvious that the oil is distinguishable at near range, but also that the values for clean sea is rapidly increasing with incidence angle. Figure 6.9b supports the observation that LWR and the oil is separable from the clean sea at that incidence angle, but again, the LWR is not easily distinguished from oil.

As for figure 6.9d, the result is again clearly affected by the diagonal wave pattern. However, the values within the slicks are closer to one than the clean sea, even if parts of the waves have the same or very similar response. Also from figure 6.9e it is seen that the values for oil, Radiagreen and clean sea are very similar, mostly between ~0.7 and ~1.

The entropy is a statistical measure of the degree of randomness of the backscatter, where the maximum value of 1 means that the polarization information become nil, and the target scattering is a truly random noise process[18]. The entropy intensity values shown in figures 6.9a and 6.9d, are generally very close to 1 across the scenes, meaning that the predominant scattering process in these scenes are quite noisy, or random.

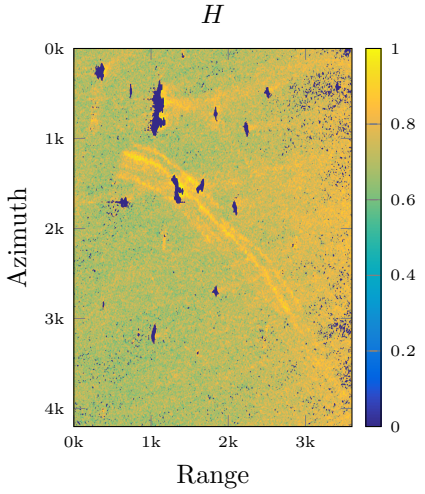

(a)

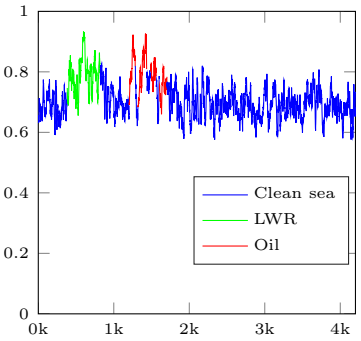

Pixel values at column number 1229

(b)

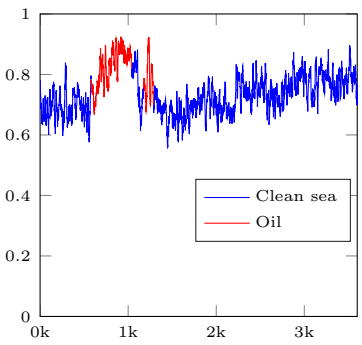

Pixel values at row number 1253

(c)

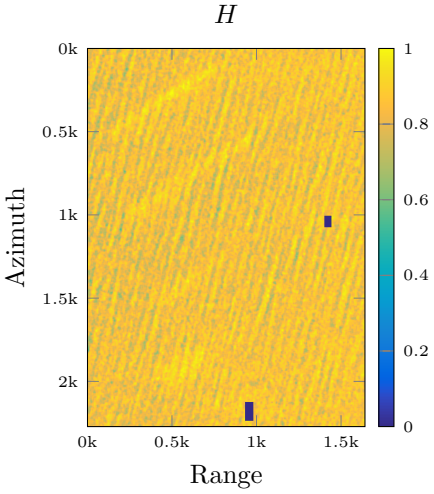

(d)

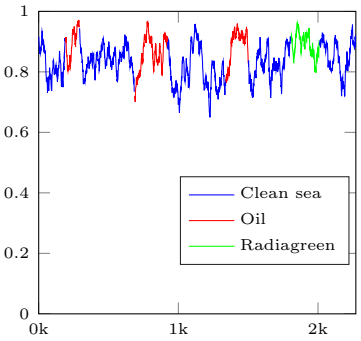

Pixel values at column number 530

(e)

Figure 6.9: (a)-(c) show the entropy, H, applied to Scene 1, and the values for H along the yellow and pink line in figure 5.2, respectively. (d) and (e) show the entropy applied to Scene 2 and the values for H along the yellow line in figure 5.4, respectively. The dark patches are NaN values where man-made objects have been masked out, while dark spots are masked out salt noise.

6.8 Feature Comparison

In this thesis, the Stokes parameters, the DoP, the χ, the H and the $m - \chi$ decomposition has been evaluated for oil slick detection using RISAT-1 FRS-1 mode.

Table 6.1 show a summary of the evaluated parameters, and the contrast between the different observed features and clean sea, based on the d_{norm} distance measure.

From the RH and RV intensity images, it is seen that the RH gives the least contrast between the observed features and the clean sea for all features, except between oil and clean sea in scene 1, where the χ is found to give the least contrast of all. RV is as expected, better than RH. However it is clear that using the Stokes parameters and its derivatives, it is possible to increase the detectability of slicks on the sea surface.

Among these parameters, the S_1 clearly distinguish itself from the rest as a consistent and powerful (compared to the rest) parameter for oil slick detection. It has the biggest contrast between the observed feature and the clean sea for all the evaluated scenarios, except between LWR and clean sea in scene 1, for which the H has got the highest contrast. The S_4 and the H also performs well over-all.

The χ has by several articles been characterized as a difficult parameter, which has a tendency of giving variable results. In this thesis, the χ is found to give very poor results for both of the considered scenes, and was by far the least usable HP parameter.

Chapter 7

Conclusion

In this thesis, two RISAT-1 FRS-1 HP scenes have been used to investigate several HP parameters for oil spill detection, and one decomposition. Previous studies on HP mode and HP polarimetric parameters have mostly depended on HP data simulated from QP data, as the access to actual HP data so far has been very limited. This thesis is therefore amongst the first to evaluate HP performance using actual HP data.

A noise analysis was performed on the evaluated scenes, from where the values of both scenes were found to be very close to, or below the NESZ. All mean values are also below the limit of 6 dB above the NESZ, defined by Minchew et al.[28], which means that according to Minchew et al.[28], the values are affected by the system noise.

For scene 1, slick detection is quite easy, with good initial contrast between slicks and the sea. Still, there are some speckle noise which disturbs the values, and there are also a lot of man-made objects in the image which impacts the dynamic range. In scene 2 however, there is a naturally occurring wave pattern, which has about the same intensity values as the oil slicks and look-alike (Radiagreen). This wave pattern makes detection much more difficult, especially for automatic detection algorithms, as also the shape and orientation will have to be accounted for. If the slicks in this scene had been of similar width and orientation as the wave pattern, detection would have been very difficult even for a skilled SAR analyst.

It is observed, as was expected, that RH has a lower backscatter intensity range than RV. The RH intensity is actually showing the smallest contrast between the slicks and the clean sea over-all (as indicated in table 6.1). The parameter

which gave the best contrast in general looking at the distance measure and visual contrast, was the S_1 parameter. The entropy has the highest contrast between the LWR region in scene 1, and clean sea, but otherwise the S_1 is dominant.

The DoP is a measure for how polarized the EM wave is. The result in this thesis show that the oil is more depolarized than the clean sea. It also shows that the clean sea values get more depolarized towards far range. This is more obvious in scene 1 than in scene 2, but scene 2 has got a much narrower incidence range than scene 2 (i.e., when looking at the evaluated sub-scenes). The parameter is useful for oil spill detection, but is outperformed by S_1 by quite a margin in most cases that has been evaluated in this thesis.

The χ is not at all effective when applied to the evaluated scenes. By visual inspection, it is not possible to detect any sign of slicks in the scenes, the entire scene is more or less flat. This parameter has previously been characterized as somewhat mysterious. The changing behaviour could e.g. be caused by the vicinity to the NESZ, incidence angles, slick characteristics, mode, sensor characteristics etc. However, it has not been possible yet to determine what actually causes the changes in the performance and behaviour of this parameter, and more research should definitely be put into explaining this.

The $m-\chi$ is the combination of the DoP and the χ. The interpretation was based on a composite RGB image, and both the RGB image and the individual channels were evaluated. The RGB image is not usable for visual interpretation, however looking at the intensity value along range, it is seen that there is a dampening over the oil slick in scene 1. However, in azimuth, it appears that the slicks, the LWR and the clean sea appear to have the same value range, thus in this range, automatic separation through thresholds may be very difficult. The best channel for distinguishing oil from clean sea is the blue channel (for both scenes), which in this context indicates single-bounce (and Bragg) backscattering. The second best is the red channel, which corresponds to double-bounce, and the least effective is the green channel, representing the randomly polarized constituents. In the blue channel, some threshold method could work for most of the slicks, but it is observed from the intensity values that some oil may be ”hidden” in the background if using an automatic threshold method.

The entropy is the measure of scatter randomness. The extreme values are inverse of the DoP extremes, i.e. when $m = 1$, then $H = 0$ and vice versa. It is also observed that for the entropy, the oil has a higher value than the clean sea, and a value which lies close to 1. This means that the oil is closing towards becoming a truly random noise process. Or in other words, that the wave is getting more depolarized. The clean sea backscatter however is less randomized and consequently

also more polarized.

None of the parameters investigated in this thesis showed any clear difference between the different concentrations of oil, nor between oil and look-alikes, when looking at their visual contrast and the distance measure d_{norm}. However, detection of slicks on the sea surface is still possible for all the evaluated parameters, except for χ.

The potential and actual behaviour of the HP mode is still just barely investigated. A massive effort to understand the mode's capabilities and limitations is urgent and required. From working on this thesis, the author get the impression that there are still some weaknesses with the RISAT-1 sensor, especially the relatively high NESZ which easily can result in a poor SNR, but also that the HP mode has got great potential for oil spill detection, and possibly also characterization based on the literature study for this thesis. It is to be noted, that the results in this thesis are based on two particular scenes, and that the results could have been completely different for other scenes where perhaps the SNR was better, the weather conditions different, other slick types and thickness, other incidence angles, etc. More research should go into checking the outcome of different variations of the mentioned conditions.

HP SAR is often fronted as an alternative to QP SAR due to its capability of large swath width. However, as resolution and swath width is very much linked, there are two possible approaches here. One option is to increase the swath width to match SP, but to keep the resolution at "QP level". Or, it is possible to increase the resolution, but then achieve a swath width that is comparable to QP. Or of course, a compromise between the two. As a trained SAR analyst with several years experience from working in 24/7 oil spill detection operations at KSAT, it is somewhat strange to see that RISAT-1 only offers the higher resolution option. For operational oil spill detection, large ground coverage is nearly always preferable to high resolution. The exception be if the oil slick's location is already known, and continuous monitoring over a limited, small area is required. The common scenario though, is that the purpose of the analysis is to detect previously undiscovered slicks, be it legal, illegal, man-made or natural. To add polarimetric information to large ground coverage could potentially offer a huge improvement to slick classification. Therefore, for the purpose of operational oil spill detection services, the larger ground coverage would have been preferable.

7.1 Future Work

The scenes evaluated in this thesis have both a very low SNR. To fully understand the performance of HP SAR, RISAT-1, and the impact that the polarimetric information could have on oil slick analysis, many more scenes should be evaluated. For such statistics, scenes containing confirmed oil slicks, with sufficient in-situ data is needed. This may be difficult, and it may take time to collect, but it is well worth the wait and effort.

There are also RADARSAT-2 scenes from approximately the same time covering the areas that are covered by the scenes evaluated in this thesis. A comparison between the performance of RADARSAT-2 and that of RISAT-1, and belonging QP and HP parameters would be of interest.

The industry should work towards increasing the ground coverage of polarimetric SAR modes. Currently, oil spill analysis is more often than not performed using modes such as RISAT-1 Medium Resolution ScanSAR mode (MRS) and Coarse Resolution ScanSAR mode (CRS), which has higher ground coverage, but which lacks the polarimetric information.

It would be useful to investigate further the physical scattering properties of oil slicks and clean sea for circular polarized incident waves. This should also be compared to the scattering properties already studied for QP mode.

Table 4.1 shows several HP parameters that has not been evaluated in this thesis. It is certainly useful to do a study of each and every one of these.

This thesis did not consider reconstruction. Reconstruction of the QP covariance matrix is an alternative to using the Stokes vector. Although it is more computationally inefficient, it is needed for certain applications and calculation of certain parameters. It should therefore be performed an evaluation of reconstruction of the QP covariance matrix from actual HP data. To the author's knowledge, this has not yet been done.

References

[1] T. L. Ainsworth, J. Kelly, J. S. Lee, and J. S. Lee. Polarimetric analysis of dual polarimetric sar imagery. In *Synthetic Aperture Radar (EUSAR), 2008 7th European Conference on*, pages 1–4, June 2008.

[2] G. Atteia and M. J. Collins. On the use of compact polarimetry {SAR} for ship detection. {*ISPRS*} *Journal of Photogrammetry and Remote Sensing*, 80(0):1 – 9, 2013. ISSN 0924-2716. doi: http://dx.doi.org/10.1016/j.isprsjprs.2013.01.009. URL `http://www.sciencedirect.com/science/article/pii/S0924271613000294`.

[3] C. Brekke and A. H. Solberg. Oil spill detection by satellite remote sensing. *Remote Sensing of Environment*, 95(1):1 – 13, 2005. ISSN 0034-4257. doi: http://dx.doi.org/10.1016/j.rse.2004.11.015. URL `http://www.sciencedirect.com/science/article/pii/S0034425704003724`.

[4] C. Brekke, V. Kudryavtsev, A.-B. Salberg, S. Skrunes, S. Ermakov, M. Migliaccio, and B. Holt. Current advances in SAR remote sensing of oil slicks and a look-ahead. In *SeaSAR 2012*, 2012.

[5] F. J. Charbonneau, B. Brisco, R. K. Raney, H. McNairn, C. Liu, P. E. Vachon, J. Shang, R. DeAbreu, C. Champagne, A. Merzouki, and T. Geldsetzer. Compact polarimetry overview and applications assessment. *Canadian Journal of Remote Sensing: Journal Canadien de télédétection*, 36:sup2:298–315, 2010. doi: 10.5589/m10-062. URL `http://dx.doi.org/10.5589/m10-062`.

[6] S. Cloude. *Polarisation: Applications in Remote Sensing*. Oxford University Press, 2009. ISBN 978-0-19-956973-1.

[7] M. J. Collins, M. Denbina, and G. Atteia. On the reconstruction of quad-pol SAR data from compact polarimetry data for ocean target detection. *IEEE, Transactions on Geoscience and Remote Sensing*, 51(1):591–600, January 2013.

[8] E. V. O. S. T. Council. Status of restoration. `http://www.evostc.state.ak.us/index.cfm?FA=status.lingering`, 2015.

[9] I. G. Cumming and F. H. Wong. *Digital Processing of Synthetic Aperture Radar Data*. Artech House, Inc., 685 Canton Street, Norwood, MA 02062, 1 edition, 2005. ISBN 1-58053-058-3.

[10] A. Danklmayer, B. J. Doring, M. Schwerdt, and M. Chandra. Assessment of atmospheric propagation effects in sar images. *IEEE Transactions on Geoscience and Remote Sensing*, 47(10):3507–3518, Oct 2009. ISSN 0196-2892. doi: 10.1109/TGRS.2009.2022271.

[11] C. Elachi and J. van Zyl. *Introduction to the Physics and Techniques of Remote Sensing*. Wiley-Interscience, John Wiley & Sons, Inc., Hoboken, New Jersey, 2nd edition, 2006. ISBN 978-0-471-47569-9.

[12] A. Guissard. Mueller and kennaugh matrices in radar polarimetry. *IEEE, Transactions on Geoscience and Remote Sensing*, 32(3):590–597, May 1994. ISSN 0196-2892. doi: 10.1109/36.297977.

[13] I. Hajnsek and K. Papathanassiou. Polsarpro manual, rough surface scattering models. Technical report, European Space Agency, Jan 2005.

[14] Jayasri, Sundari, Kumari, and Prasad. Study of oil spill in norwegian area using decomposition techniques on RISAT-1 hybrid polarimetric data. *The International Archives of the Photogrammetry, Remote Sensing and Spatial Information Sciences*, XL-8:1043–1048, 2014.

[15] L. Kumar, J. Kishore, and P. Rao. Unsupervised classification based on decomposition of RISAT-1 images for oil spill detection. In *Advances in Computing, Communications and Informatics (ICACCI), 2013 International Conference on*, pages 739–746, Aug 2013. doi: 10.1109/ICACCI.2013.6637266.

[16] L. J. V. Kumar, D. J. Kishore, and D. P. K. Rao. Decomposition methods for detection of oil spills based on RISAT-1 SAR images. *International Journal of Remote Sensing & Geoscience (IJRSG)*, 3:1–10, July 2014. ISSN 2319-3484.

[17] M. Lavalle, D. Solimini, E. Pottier, and Y. L. Desnos. Compact polarimetric sar interferometry. *IET Radar, Sonar Navigation*, 4(3):449–456, June 2010. ISSN 1751-8784. doi: 10.1049/iet-rsn.2009.0049.

[18] J.-S. Lee and E. Pottier. *Polarimetric Radar Imaging: From Basics to Applications*. CRC Press, Taylor & Francis Group, 6000 Broken Sound Parkway NW, Suite 300, Boca Raton, FL 33487-2742, 2009. ISBN 978-1-4200-5497-2.

[19] H. Li, W. Perrie, Y. He, S. Lehner, and S. Brusch. Target detection on the ocean with the relative phase of compact polarimetry SAR. *IEEE, Transactions on Geoscience and Remote Sensing*, 51(6):3299–3305, June 2013. ISSN 0196-2892. doi: 10.1109/TGRS.2012.2224119.

[20] H. Li, W. Perrie, Y. He, J. Wu, and X. Luo. Analysis of the polarimetric SAR scattering properties of oil-covered waters. *IEEE, Journal of Selected topics in Applied Earth Observations and Remote Sensing*, PP(99), October 2014. ISSN 1939-1404.

[21] H. Li, W. Perrie, Y. Zhou, and Y. He. Oil spill detection on the ocean surface using hybrid polarimetric sar imagery. *Science China Earth Science*, 59:249–257, 7 2015. doi: 10.1007/s11430-015-5152-0.

[22] Y. Li, Y. Zhang, J. Chen, and H. Zhang. Improved compact polarimetric SAR quad-pol reconstruction algorithm for oil spill detection. *IEEE, Geoscience and Remote Sensing Letters*, 11(6):1139–1142, June 2014. ISSN 1545-598X. doi: 10.1109/LGRS.2013.2288336.

[23] Y. Li, H. Lin, Y. Zhang, and J. Chen. Comparisons of circular transmit and linear receive compact polarimetric SAR features for oil slicks discrimination. *Journal of Sensors*, 2015, April 2015.

[24] T. M. Lillesand, R. W. Kiefer, and J. W. Chipman. *Remote Sensing and Image Interpretation*. John Wiley & Sons, Inc, 111 River Street, Hoboken, NJ 07030-5774, 6 edition, 2007. ISBN 978-0-470-05245-7.

[25] P. Liu, X. Li, J. J. Qu, W. Wang, C. Zhao, and W. Pichel. Oil spill detection with fully polarimetric UAVSAR data. *Marine Pollution Bulletin*, 62 (12):2611 – 2618, 2011. ISSN 0025-326X. doi: http://dx.doi.org/10.1016/j.marpolbul.2011.09.036. URL `http://www.sciencedirect.com/science/article/pii/S0025326X11005248`.

[26] M. L. Loureiro, E. Ojea, A. Ribas, and E. L. Iglesias. Estimated costs and admissible claims linked to the prestige oil spill. *Ecological Economics*, 59: 48–63, 2006. doi: 10.1016/j.ecolecon.2005.10.001.

[27] *RADARSAT-2 Product Description*. MacDonald, Dettwiler and Associates Ltd. (MDA), 1/11 edition, May 2014.

[28] B. Minchew, C. Jones, and B. Holt. Polarimetric analysis of backscatter from the deepwater horizon oil spill using L-band synthetic aperture radar. *Geoscience and Remote Sensing, IEEE Transactions on*, 50(10):3812–3830, Oct 2012. ISSN 0196-2892. doi: 10.1109/TGRS.2012.2185804.

[29] F. Nunziata, M. Migliaccio, and X. Li. Sea oil slick observation using hybrid-polarity SAR architecture. *IEEE Journal of Oceanic Engineering*, 40(2): 426–440, April 2015.

[30] N. Otsu. A threshold selection method from gray-level histograms. *IEEE Transactions on Systems, Man, and Cybernetics*, SMC-9(1):6266, Jan 1979.

[31] W. H. Peake and T. L. Oliver. The response of terrestrial surfaces at microwave frequencies. Technical Report Technical Report AFAL-TR-70-301, ElectroScience Laboratory, The Ohio State University, Columbus, Ohio, May 1971.

[32] J. L. Ramseur. Deepwater Horizon Oil Spill: Recent activities and ongoing developments, April 2015.

[33] R. Raney. Synthetic aperture radar hybrid-quadrature-polarity method and architecture for obtaining the stokes parameters of radar backscatter, Sept. 4 2012. URL `https://www.google.no/patents/US8258996`. US Patent 8,258,996.

[34] R. K. Raney. Dual-polarized SAR and Stokes parameters. *IEEE Geoscience and Remote Sensing Letters*, 3(3):317–319, July 2006.

[35] R. K. Raney. Hybrid-polarity SAR architecture. *IEEE Transactions on Geoscience and Remote Sensing (TGRS)*, 45(11), November 2007.

[36] R. K. Raney, J. T. Cahill, G. W. Patterson, and D. B. Bussey. The m-chi decomposition of hybrid dual-polarimetric radar data. In *Geoscience and Remote Sensing Symposium (IGARSS), 2012 IEEE International*, pages 5093–5096. IEEE, July 2012. ISBN 978-1-4673-1160-1.

[37] R. K. Raney, A. Freeman, and R. L. Jordan. Improved range ambiguity performance in quad-pol SAR. *IEEE Transactions on Geoscience and Remote Sensing*, 50(2):349–356, February 2012.

[38] R. K. Raney, A. Freeman, and R. L. Jordan. Improved range ambiguity performance in quad-pol SAR. *IEEE Transactions on Geoscience and Remote Sensing*, 50(2):349–356, February 2012. ISSN 0196-2892. doi: 10.1109/TGRS.2011.2121075.

[39] O. o. t. M. A. Republic of the Marshall Islands. Deepwater horizon marine casualty investigation report. `http://www.register-iri.com/forms/upload/Republic_of_the_Marshall_Islands_DEEPWATER_HORIZON_Marine_Casualty_Investigation_Report-Low_Resolution.pdf`, August 2011.

[40] A.-B. Salberg, Øystein Rudjord, and A. H. Solberg. Oil spill detection in hybrid-polarimetric SAR images. *IEEE Transactions on GeoScience and Remote Sensing (TGRS)*, 52, January 2014. ISSN 0196-2892.

[41] R. A. Schowengerdt. *Remote Sensing: Models and Methods for Image Processing*. Academic Press, 3 edition, 2006. ISBN 978-0-0804-8058-9.

[42] J. Shang, H. McNairn, F. Charbonneau, Z. Chen, and X. Jiao. Sensitivity analysis of compact polarimetry parameters to crop growth using simulated radarsat-2 sar data. In *2012 IEEE International Geoscience and Remote Sensing Symposium*, pages 1825–1828, July 2012. doi: 10.1109/IGARSS.2012.6351156.

[43] R. Shirvany, M. Chabert, and J.-Y. Tourneret. Ship and oil-spill detection using the degree of polarization in linear and hybrid/compact dual-pol SAR. *IEEE Journal of Selected Topics in Applied Earth Observations and Remote Sensing*, 5(3):885–892, 2012. ISSN ISSN 1939-1404.

[44] S. Skrunes, C. Brekke, and T. Eltoft. Characterization of marine surface slicks by radarsat-2 multipolarization features. *Geoscience and Remote Sensing, IEEE Transactions on*, 52(9):5302–5319, Sept 2014. ISSN 0196-2892. doi: 10.1109/TGRS.2013.2287916.

[45] A. H. S. Solberg, G. Storvik, R. Solberg, and E. Volden. Automatic detection of oil spills in ers sar images. *IEEE Transactions on Geoscience and Remote Sensing*, 37(4):1916–1924, Jul 1999. ISSN 0196-2892. doi: 10.1109/36.774704.

[46] J.-C. Souyris, P. Imbo, R. Fjørtoft, S. Mingot, and J.-S. Lee. Compact polarimetry based on symmetry properties of geophysical media: The $\pi/4$ mode. *IEEE Transactions on Geoscience and Remote Sensing*, 43(3), March 2005.

[47] F. T. Ulaby, R. K. Moore, and A. K. Fung. *Microwave Remote Sensing: Active and Passive*, volume 2. Reading, Mass. : Addison-Wesley, 1982. ISBN 9780890061923.

[48] G. R. Valenzuela. Theories for the interaction of electromagnetic and oceanic waves a review. *Boundary-Layer Meteorology*, 13(1-4):61–85, 1978. ISSN 0006-8314. doi: 10.1007/BF00913863. URL `http://dx.doi.org/10.1007/BF00913863`.

[49] J. van Zyl and Y. Kim. *Synthetic Aperture Radar Polarimetry*. JPL Space Science and Technology Series. John Wiley & Sons, Inc., 1 edition, 2011. ISBN 978-1-118-11511-4.

[50] L. Xie, H. Zhang, C. Wang, F. Wu, B. Zhang, and Y. Tang. Maritime application using $h-\alpha$ decomposition in compact and dual-pol sar. In *Asia-Pacific Conference on Synthetic Aperture Radar (APSAR), 2013*, pages 563–566, September 2013.

[51] L. Xie, H. Zhang, C. Wang, and Z. Shan. Similarity analysis of entropy/alpha decomposition between hh/vv dual- and quad-polarization sar data. *Remote Sensing Letters*, 6(3):228–237, 2015. doi: 10.1080/2150704X.2015.1026954.

[52] J. Yin, J. Yang, Z. Zhou, and J. Song. The extended Bragg scattering model-based method for ship and oil-spill observation using compact polarimetric SAR. *Selected Topics in Applied Earth Observations and Remote Sensing, IEEE Journal of*, PP(99):1–13, 2015. ISSN 1939-1404. doi: 10.1109/JSTARS.2014.2359141. Reviewed and accepted for publishing.